

We are IntechOpen, the world's leading publisher of Open Access books Built by scientists, for scientists

6,300

Open access books available

171,000

International authors and editors

190M

Downloads

Our authors are among the

154

Countries delivered to

TOP 1%

most cited scientists

12.2%

Contributors from top 500 universities



WEB OF SCIENCE™

Selection of our books indexed in the Book Citation Index
in Web of Science™ Core Collection (BKCI)

Interested in publishing with us?
Contact book.department@intechopen.com

Numbers displayed above are based on latest data collected.
For more information visit www.intechopen.com



Kerosene-Water Multiphase Flow in Vertical and Inclined Pipes

Faik Hamad, Nadeem Ahmed Sheikh and Muzaffar Ali

Abstract

This chapter presents the volume fraction distribution of kerosene-water two-phase flow in vertical and inclined pipes. The study of liquid-liquid two-phase flow is very significant to oil industry and many other processes in industry where two liquids are mixed and flow together. Pitot tube and optical probes are used for the measurement of velocity of water and volume fraction. The experimental measurements of the local parameters demonstrate that the single-phase and two-phase flows reached the fully developed axisymmetric conditions at $L/D \geq 48$ (L , pipe length; D , pipe diameter). The results also showed the severe asymmetry distributions of the volume fraction at the entrance region ($L/D = 1$) downstream the bend and in the inclined pipe. The comparison of volume fraction profiles with void fraction profiles indicated a significant difference in their shapes. The results also showed that the kerosene accumulated at the upper wall of the inclined pipe and the distribution improved by increasing the volumetric quality.

Keywords: volume fraction, kerosene-water two-phase flow, vertical and inclined pipes, optical probe, pitot tube

1. Introduction

Multiphase flows are important for the design of steam/water flow in steam generators, jet engines, condensers, extraction and distillation processes, gas and oil mixture in pipelines, and refrigeration systems. The mixture of two immiscible liquids is characterized by the existence of interfaces between the two fluids, associated with a discontinuity of properties across the interface. The single-phase flow is traditionally classified into laminar, transitional, and turbulent flows according to the flow Reynolds number. The two-phase flow in vertical pipe can be classified, according to the geometry of the interfaces.

The primary condition for all two-phase flows is specified by the volumetric quality β , which is defined as:

$$\beta = \frac{Q_d}{Q_c + Q_d} \quad (1)$$

where Q_d is the flow rate of the dispersed phase and Q_c is the flow rate of the continuous phase.

For a pipe of radius R , the corresponding (area averaged) superficial velocities are defined as:

Continuous phase superficial velocity:

$$\bar{U}_{cs} = \frac{Q_c}{\pi R^2} \quad (2)$$

Dispersed phase superficial velocity:

$$\bar{U}_{ds} = \frac{Q_d}{\pi R^2} \quad (3)$$

For both gas-liquid and liquid-liquid flow systems, the continuous phase is usually water.

In spite of the large number of published work in multiphase flow area, the publication on using local probe measurements for liquid-liquid flow is very limited compared to the gas-liquid two-phase flow. The purpose of this chapter is to publish some data on volume fraction profiles for liquid-liquid flow in vertical and inclined pipes. The following data are presented in this chapter: (i) the void fraction distribution for gas-liquid two-phase flow in vertical pipe, (ii) the volume fraction distribution for flow development of kerosene-water flow in vertical pipe, and (iii) the volume fraction distribution for the fully developed kerosene-water flow in vertical and inclined pipes.

2. Void fraction/volume fraction definition

Most experimental results for the void fraction α (volume fraction for liquid-liquid flow) have been obtained by a point sensor, which was used to discriminate in time between the two phases. Experimentally the void fraction α has been evaluated from the time record from such a probe as:

$$\alpha = \frac{\sum \Delta t_d}{T} \quad (4)$$

where $\sum \Delta t_d$ is the time the probe is located in the dispersed phase and T is the total sampling time used for record. It should be noticed that in many investigations, reference is made to the (average) void fraction $\bar{\alpha}$. The proper reference would have been the volumetric quality (β) obtained for gas-liquid systems by the quick closing valve method, X-ray or neutron techniques. For liquid-liquid systems, β can be obtained by measuring the two flow rates Q_d and Q_c .

Experimental studies of the phase distributions in concurrent two-phase upflow in vertical pipes present a complex picture that has not yet been systematically evaluated. The common flow patterns for vertical upward flow, in which both phases flow upwards in a circular tube, are shown in **Figure 1**. As the volume flow rate of gas increased for constant water flow rate, the flow patterns would vary. The following types of flow patterns can be found in vertical pipes:

- i. Bubbly flow: bubbles of gas or liquid in a continuous liquid phase appear, and the size of the bubbles can be very small or large.
- ii. Slug flow: in this type a bullet-shaped plug of gas is formed from many bubbles concentrated in one part to make larger bubbles, which approach the diameter of the pipe. The liquid phase is in continuous flow.
- iii. Churn flow: braking down of large vapor bubbles in plug flows form the churn flow. This is a highly oscillatory flow, and there is tendency for each phase to be continuous with irregular interfaces.

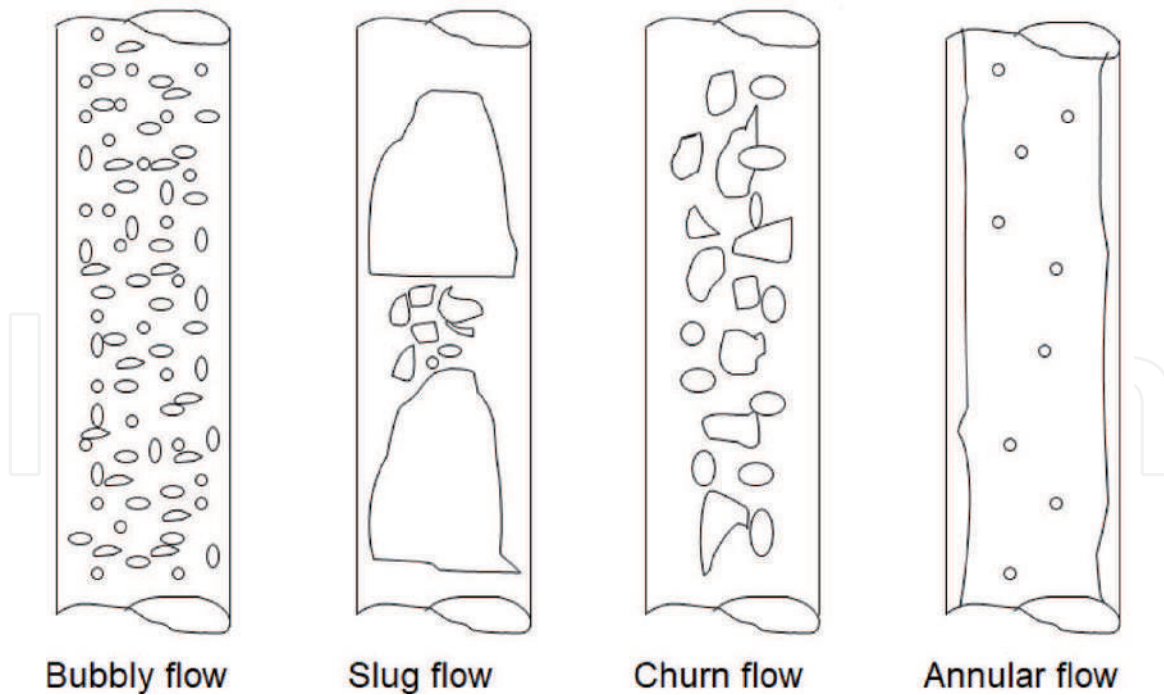


Figure 1.
 Flow patterns in vertical upward flow in a pipe [1].

- iv. Annular flow: the liquid forms a film around the wall of the tube. The gas phase flows in the centre.

3. Gas: liquid void fraction distribution in vertical pipes

A significant number of measurements have been made for upflow in vertical pipes. Several investigators, e.g. Malnes [2], Serizawa et al. [3], Michiyoshi and Serizawa [4], Wang et al. [5] and Liu and Bankoff [6], have observed the peaking phenomenon of the local void fraction near the wall as shown in **Figure 2**. Some investigators, such as Van der Welle [7], Moujaes and Dougall [8] and Johnson and White [9], have observed a maximum void fraction at the centreline as shown in **Figure 3**. Other researchers, such as Nakoryakov et al. [10], Spindler et al. [11] and

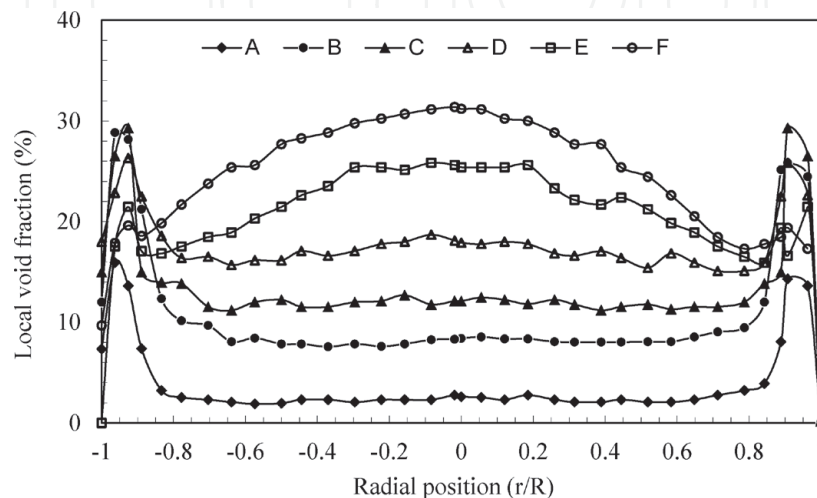


Figure 2.
 Void fraction distributions for air-water upflow in a pipe with a continuous phase mean velocity = 1.03 m/s, $Z/D = 30$. A-D are bubbly flow, and E and F are slug flow [3].

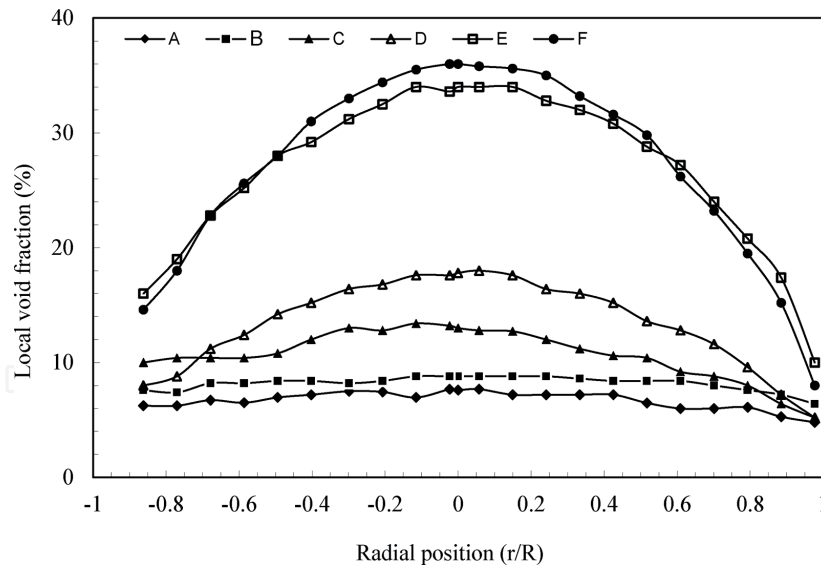


Figure 3. Void fraction distributions for air-water upflow in a pipe with different flow rates, $Z/D = 42.5$. A–D are bubbly flow, and E and F are transitional flow [9].

Liu [12], observed both wall and centreline peaking void fraction distributions for two-phase flow. The actual void fraction distribution configurations have been found to depend on the initial conditions: bubble size and flow rates, physical properties of the fluids, and the test section condition geometry.

4. Liquid: liquid volume fraction

Compared to the large number of publications on gas-liquid flows, less work have been published on liquid-liquid flows.

Most of the papers on liquid-liquid mixture flow were published by research group at the University of Bradford ([13, 14]; Hamad et al. [15]; Hamad and Bruun [16]). Most of these papers focused on the development of optical techniques for kerosene-water upward flow in vertical pipes. However, Farrar and Bruun [13] highlighted the problem of the severe asymmetry, and the swirl generated upstream the inlet due the existence of 90° bend as part of the experimental facility.

Zhao et al. [17] used a double-sensor conductivity probe to measure the local oil phase fraction distribution for flow in a vertical pipe at $L/D = 72$. They found that the volume fraction profiles were uniform for $\beta < 9.2\%$ and changed into wall peak for $\beta > 9.2\%$. The local oil phase fraction profiles at (a) constant water flow rate ($J_w = 0.33$ m/s) and (b) constant oil flow rate ($J_o = 0.066$ m/s) are given in **Figure 4**.

A comprehensive experimental data on kerosene-water two-phase flow were published by Hamad et al. [18, 19] and Hamad et al. [20] in vertical and inclined pipes. A summary of the results from each paper is given in the following sections.

4.1 Development of kerosene-water flow in vertical pipe

Hamad et al. [18] studied the flow development in a vertical pipe of 77.8 mm inner diameter and 4500 mm length downstream of a 90° bend experimentally at $L/D = 1, 16, 38$ and 54 using the experimental facility in **Figure 5**. Single-phase (water) flow measurements were made to check the establishment of fully developed symmetrical flow conditions. **Figure 6** shows the radial distribution of axial velocity in the plane parallel to the bend at different L/D ratios. Two values of \bar{u}_{ws}

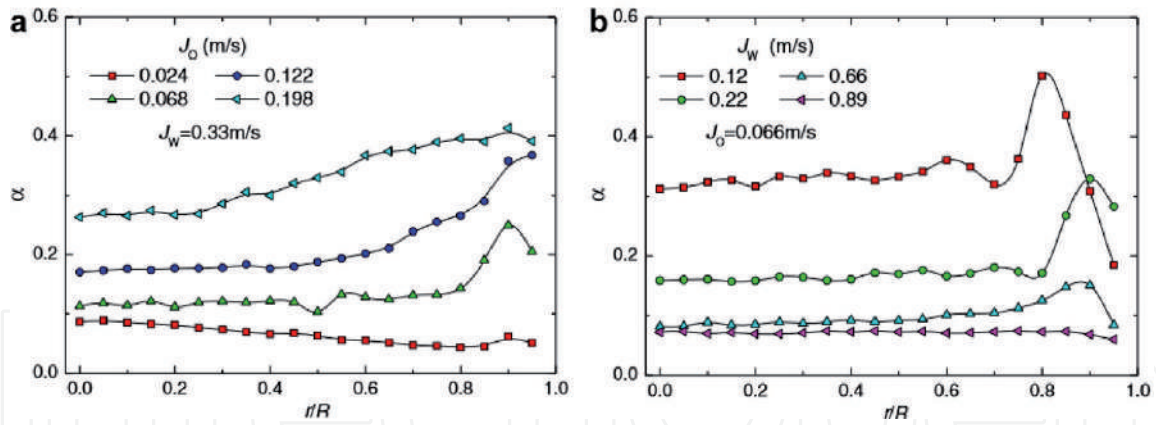


Figure 4. Oil volume fraction profiles at (a) constant water flow rate ($J_w = 0.33 \text{ m/s}$) and (b) constant oil flow rate ($J_o = 0.066 \text{ m/s}$) [17].

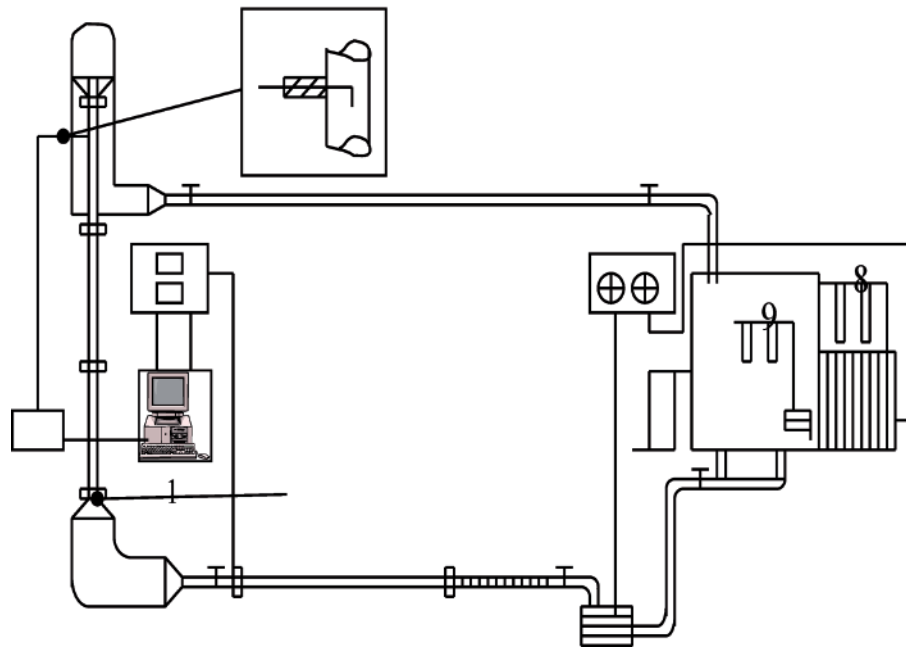


Figure 5. Schematic diagram of two-phase flow experimental facility [18].

are used (0.44 m/s ($Re = 33,800$) and 0.77 m/s ($Re = 60,000$)). The results show that water velocity distributions become fully developed at $L/D > 48$. The empirical power law velocity distribution given in Eq. (5) for single-phase turbulent flow [21, 22] was also included in **Figure 6** to confirm the accuracy of the measurements:

$$\bar{U} = \bar{U}_{cl} (1 - r/R)^{1/n} \quad (5)$$

Then, the kerosene was introduced to perform volume fraction measurements using optical probe [14] at four different axial positions at $L/D = 1, 16, 38$ and 54 downstream of the pipe bend. Three different flow conditions are considered: Case 1: water superficial velocity, $\bar{u}_{ws} = 0.44 \text{ m/s}$, and volumetric quality, $\beta = 9.2\%$; Case 2: $\bar{u}_{ws} = 0.44 \text{ m/s}$ and $\beta = 18.6\%$ and one high \bar{u}_{ws} condition; and Case 3: $\bar{u}_{ws} = 0.77 \text{ m/s}$ and $\beta = 18.6\%$. For Case 1, the axisymmetric distribution is very poor at $L/D = 1$ (**Figure 7(a)**) with high volume fraction values of 20% near the inner side of the bend to the lower value near the outer wall of the bend of 4%. For Case 2, increasing β to 18.6% for the same \bar{u}_{ws} (**Figure 7(a)**) improves the axisymmetric distribution across the pipe. For Case 3, the axisymmetric distribution improved

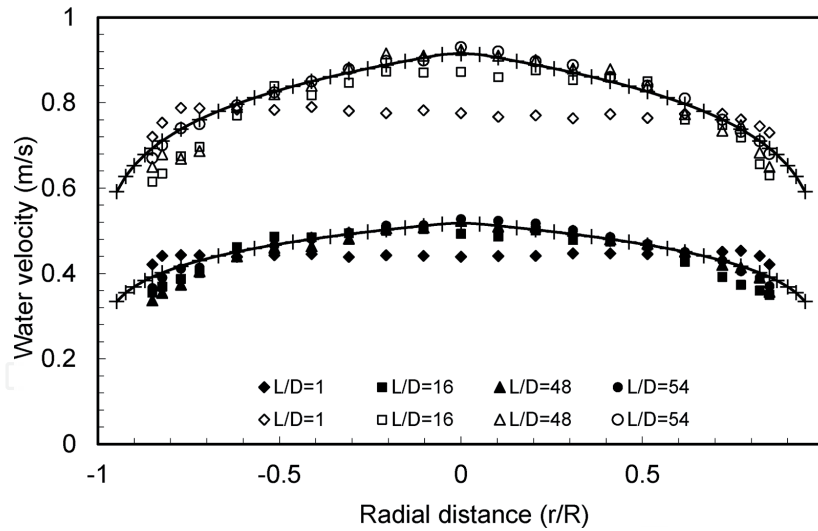


Figure 6. Local single-phase velocity distribution at different L/D ratios for average water velocity = 0.44 m/s (solid symbols) and 0.77 m/s (open symbols). The power law velocity distribution (solid line) is also included [18].

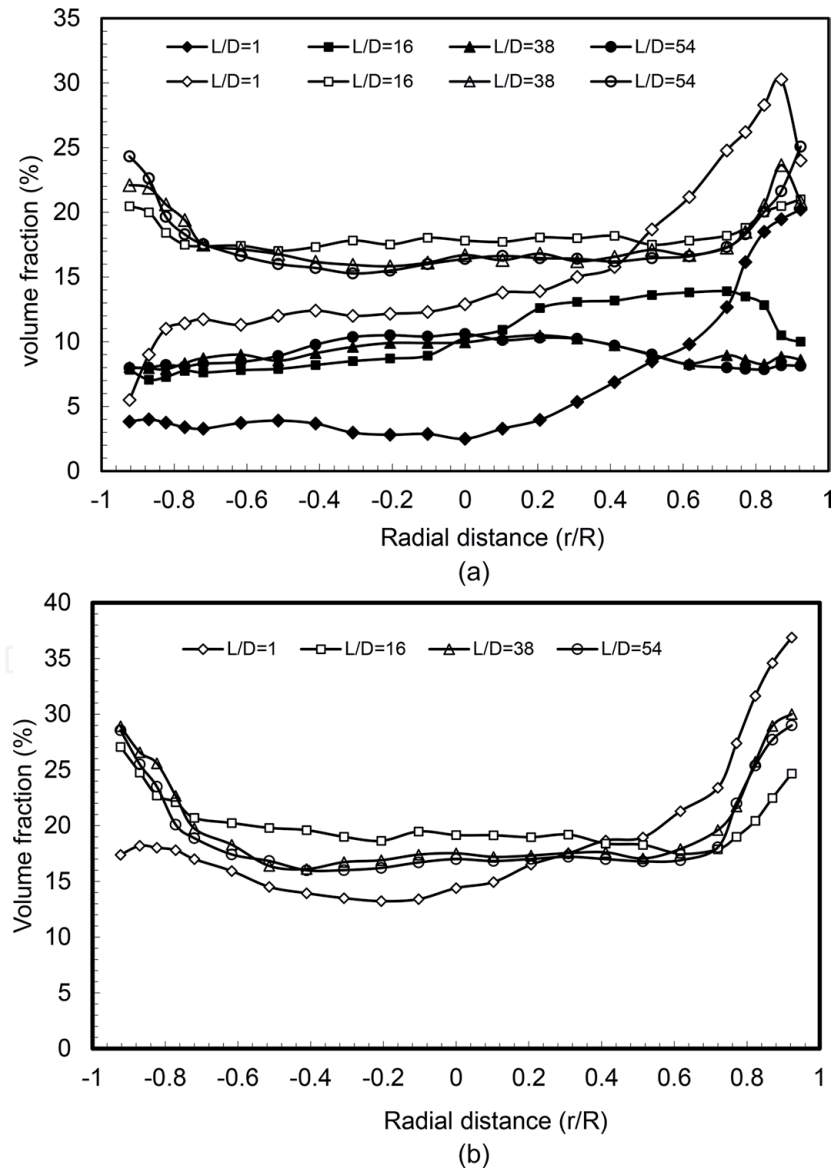


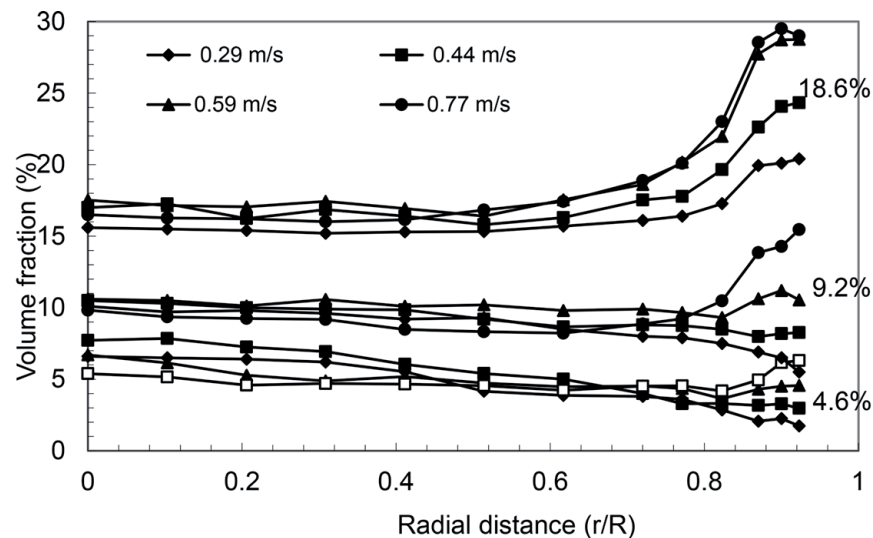
Figure 7. Volume fraction distributions at different (a) L/D for $\bar{U}_{ws} = 0.44$ m/s and $\beta = 9.2\%$ (solid symbols) and 18.6% (open symbols) [18], (b) L/D for $\bar{U}_{ws} = 0.77$ m/s and $\beta = 18.6\%$ [18].

further by increasing \bar{U}_{ws} for the same β (**Figure 7(b)**). The main conclusion is that the axisymmetric becomes better for higher β and \bar{U}_{ws} . The change in volume fraction distribution may be attributed to the improvement of the mixing process of the kerosene with water which acts against the effect of the buoyancy force and the centrifugal force at the outlet of the bend. However, the distribution becomes nearly symmetrical at $L/D = 16$. There appear to be no significant differences between the distributions at $L/D = 38$ and 54 , which suggests that fully developed, symmetrical condition was achieved.

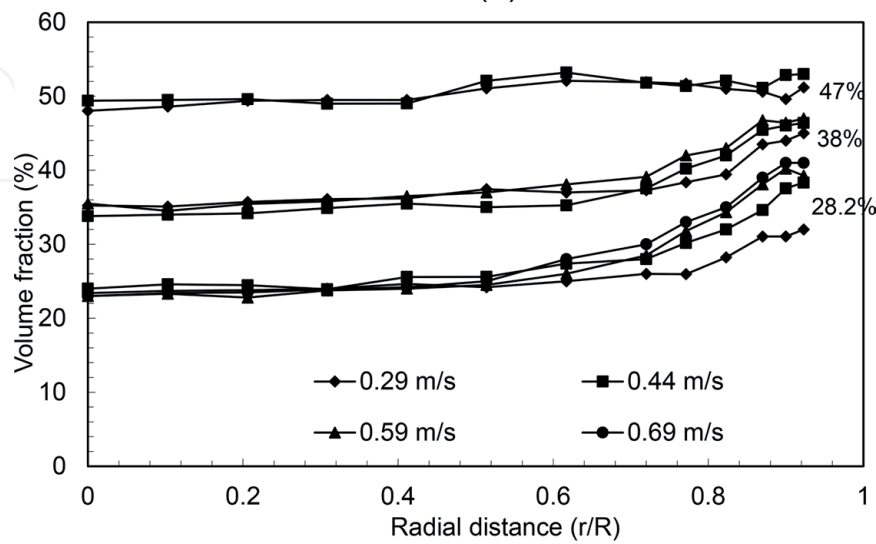
4.2 Fully developed flow of kerosene-water flow in vertical pipe

Hamad et al. [19] studied the flow of kerosene-water upward flow in a vertical pipe at ($L/D = 54$) using optical probes. The effects of \bar{U}_{ws} and β on radial volume fraction distribution $[\alpha(r)]$ of two-phase flow parameters were investigated.

The local volume fraction is calculated from the output of the leading sensor of the dual optical probe by determining the average drop residence time using the procedure described in Hamad et al. [14]. Comprehensive measurements

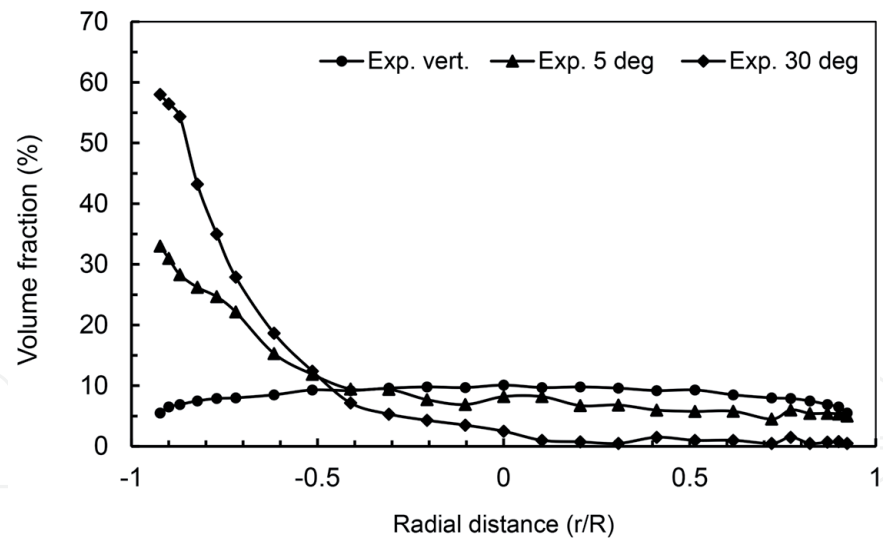


(a)

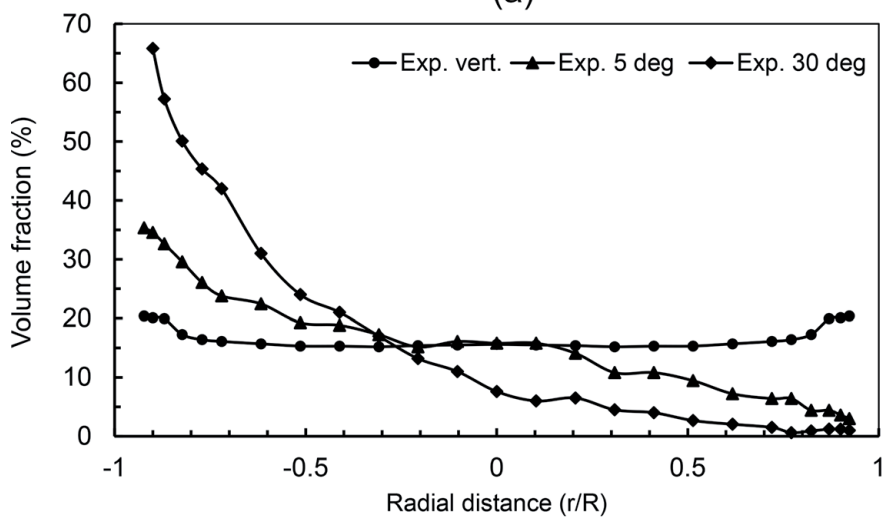


(b)

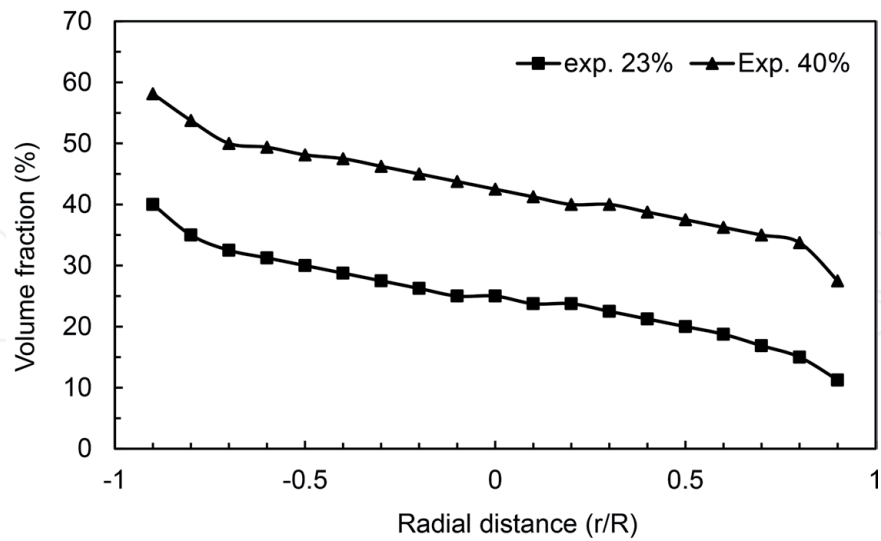
Figure 8. Volume fraction profiles for different (a) \bar{U}_{ws} and $\beta = 4.6, 9.2$ and 18.6% [19], (b) \bar{U}_{ws} and $\beta = 28.2, 38$ and 47% [19].



(a)



(b)



(c)

Figure 9.

The effect of pipe inclination on volume fraction distribution (a) ($U_{sw} = 0.29$ m/s, $\beta = 9.2\%$) [20], (b) ($U_{sw} = 0.29$ m/s, $\beta = 18.6\%$) [20]. (c) the $\alpha(r)$ distribution from Vigneaux et al. [24].

of $\alpha(r)$ were performed for a number of β values in the range of 4.6–47% and constant \bar{u}_{ws} of 0.29, 0.44, 0.59, 0.69 and 0.77 m/s. The $\alpha(r)$ profiles have been plotted together for various values of \bar{u}_{ws} for each value of β as shown in **Figure 8(a)** and **(b)**.

As the $\alpha(r)$ profile primarily reflects the kerosene content in the mixture flow, it follows that the related $\alpha(r)$ profile sets for $\beta = 4.6\%$, 9.2% , 18.6% , 28.2% , 38% and 47% are centred around these values. The graphs also show distinct variations, both within each β group and between groups with different β values.

The results from **Figure 8(a)** and **(b)** show that increasing \bar{U}_{ws} with low β ($<20\%$) will change the $\alpha(r)$ profiles from convex shape with peak at the pipe centreline to flat shape and then to concave shape with peak near the wall. For moderate β ($20\text{--}40\%$), the $\alpha(r)$ profiles have a concave shape for different \bar{U}_{ws} with peak near the wall which has high values for higher \bar{U}_{ws} . In the case of $\beta \approx 50\%$, the $\alpha(r)$ profile shapes are flat for the two cases in **Figure 8(b)**.

The $\alpha(r)$ profiles from centreline which peaked to uniform to wall peaked and then to uniform can be attributed to the change in lift force due to the change in drop diameter, slip velocity and radial velocity distribution of both phases. The present finding is supported by the results for liquid-liquid flows from Zhao et al. [17] and Hua et al. [23] for the same range of \bar{U}_{ws} and β .

4.3 Kerosene-water flow in inclined pipe

Hamad et al. [20] used an optical probe to study the kerosene-water flow inclined at 5° and 30° from vertical at $L/D = 54$. The volume fraction was measured for $\bar{U}_{ws} = 0.29$ m/s and $\beta = 9.2\%$ and 18.6% .

Figure 9(a) shows the radial $\alpha(r)$ distributions of the volume fraction, $\alpha(r)$ for 0° , 5° and 30° inclination angles at \bar{U}_{ws} of 0.29 m/s and two values of $\beta = 9.2$ and 18.6% .

The results in **Figure 9(a)** and **(b)** show that the inclination has a significant influence on the distribution of $\alpha(r)$. The kerosene drops were separated from the water accumulated at the upper zone of the pipe due to the gravity effect. The effect of increasing β in an inclined pipe leads to dispersion of the drops to the lower zone of the pipe due to the recirculation cells of the moving droplet swarms.

The present results are supported by the findings reported by Vigneaux et al. [24] and Flores et al. [25]. **Figure 9(c)** presents the two sets of experimental data reported by Vigneaux et al. [24] in a pipe inclined at 15° from vertical. In the first case, $\beta = 23\%$, and $U_{sw} = 0.27$ m/s, and in the second case, $\beta = 40\%$, and $U_{sw} = 0.21$ m/s.

5. Conclusion

The results on void fraction profiles from literature show the complexity of the flow behaviour. It is reflected in different types of profiles due to the local interaction between the bubbles and the continuous phase. This may be attributed to the various forces at interface between the phases including drag, lift and virtual force as well as the size of bubbles and compressibility effect. In contrast, the volume fraction profiles for liquid-liquid two-phase flow have similar shapes. This behaviour may be attributed to smaller drops, smaller density ratio, smaller slip velocity and the incompressible nature of the liquids.

The results show that fully developed condition for liquid-liquid flow can be achieved at lower L/D compared to gas-liquid flow. This is due to incompressible nature of liquid drops which have the same volume compared to the gas bubbles which expand continuously due to the pressure drop in flow direction.

Acknowledgements

Authors are thankful to their parent institutions for providing support for the research.

IntechOpen

Author details

Faik Hamad^{1*}, Nadeem Ahmed Sheikh² and Muzaffar Ali³

1 School of Science, Engineering, and Design, Teesside University, UK

2 Department of Mechanical Engineering, Faculty of Engineering and Technology, International Islamic University, Islamabad, Pakistan

3 Department of Energy Engineering, University of Engineering and Technology Taxila, Pakistan

*Address all correspondence to: f.hamad@tees.ac.uk

IntechOpen

© 2020 The Author(s). Licensee IntechOpen. This chapter is distributed under the terms Commons Attribution - NonCommercial 4.0 License (<https://creativecommons.org/licenses/by-nc/4.0/>), which permits use, distribution and reproduction for non-commercial purposes, provided the original is properly cited. 

References

- [1] Hamad FA. A study of the continuous and dispersed phase parameters in kerosene-water two-phase up-flow in vertical pipe [PhD Thesis]. UK: University of Bradford; 2001
- [2] Malnes D. Slip Ratios and Friction Factors in Bubble Flow Regime in Vertical Pipes, Report No. KR-100. Kjeller, Norway: Institute for Atomenergi; 1966
- [3] Serizawa A, Kataoka I, Michiyoshi I. Turbulence structure of water bubbly flow: II. Local properties. *International Journal of Multiphase Flow*. 1975;2:235-246
- [4] Michiyoshi I, Serizawa A. Turbulence in two-phase bubbly flow. *Nuclear Engineering and Design*. 1986;95:235-267
- [5] Wang SK, Lee SJ, Jones OC, Lahey RT. 3-D turbulence structure and phase distribution measurements in bubbly two-phase flow. *International Journal of Multiphase Flow*. 1987;13:327-343
- [6] Liu TJ, Bankoff SG. Structure of air-water bubbly flow in vertical pipe-11. Void fraction, bubble velocity, and bubble size distribution. *International Journal of Heat and Mass Transfer*. 1993;36:1061-1072
- [7] Van der Welle. Void fraction, bubble velocity, and bubble size in two-phase flow. *International Journal of Multiphase Flow*. 1985;11:317-345
- [8] Moujaes S, Dougall RS. Experimental investigation of cocurrent two-phase flow in a vertical rectangular channel. *Canadian Journal of Chemical Engineering*. 1987;65:705-715
- [9] Johnson AB, White DB. Experimental determination of gas migration velocities with non-Newtonian fluids. *International Journal of Multiphase Flow*. 1993;19:921-941
- [10] Nakoryakov VE, Kashinsky ON, Burdukov AP, dnoral VP. Local characteristics of upward gas-liquid flows. *International Journal of Multiphase Flow*. 1981;7:63-81
- [11] Spindler K, Bierer M, Lorenz G, Erhard A, Hahne E. Measurements in vertical gas-liquid two-phase flows using an optical fiber probe. In: *Proceedings of the First Word Conference on Experimental Heat Transfer, Fluid Mechanics and Thermodynamics*. Dubrovnik, Yugoslavia; 1988. pp. 348-357
- [12] Liu TJ. Bubble size and entrance length effects on void development in a vertical channel. *International Journal of Multiphase Flow*. 1993;19:99-113
- [13] Farrar B, Bruun HH. A computer based hot-film technique used for flow measurements in a vertical kerosene-water pipe flow. *International Journal of Multiphase Flow*. 1996;22:733-752
- [14] Hamad FA, Imberton F, Bruun HH. An optical probe for measurements in liquid-liquid two-phase flow. *Measurement Science and Technology*. 1997;8:1122-1132
- [15] Hamad FA, Bruun HH. Evaluation of bubble/drop velocity by a single normal hot-film placed in a two-phase flow. *Measurement Science and Technology*. 2000;11:11-19
- [16] Hamad FA, Pierscionek BK, Bruun HH. A dual optical probe for volume fraction, drop velocity and drop size measurements in liquid-liquid two-phase flow. *Measurement Science and Technology*. 2000;11:1307-1318
- [17] Zhao D, Guo L, Hu X, Zhang X, Wang X. Experimental study on local characteristics of oil-water dispersed

flow in a vertical pipe. *International Journal of Multiphase Flow*. 2006;**32**:1254-1268

[18] Hamad FA, He S, Khan MK, Bruun HH. Development of kerosene–water two-phase up-flow in a vertical pipe downstream of a 90° bend. *The Canadian Journal of Chemical Engineering*. 2013a;**91**(2):354-367

[19] Hamad FA, Khan MK, Bruun HH. Experimental study of kerosene–water two-phase flow in a vertical pipe using hot-film and dual-optical probe bend. *The Canadian Journal of Chemical Engineering*. 2013b;**91**(7):1296-1311

[20] Hamad FA, Albarzenji D, Ganesan p. Study of kerosene-water two-phase flow characteristics in vertical and inclined pipes. *The Canadian Journal of Chemical Engineering*. 2014;**92**(5):905-917

[21] Munson BR, Young DF, Okiishi TH. *Fundamentals of Fluid Mechanics*. 4th ed. New York, USA: John Willey & Sons, Inc; 2002

[22] Schlichting H. *Boundary Layer Theory*. New York, USA: McGraw-Hill; 1979

[23] Hua L, Mi W, Ying-Xiang W, Yi-Xin M, Richard W. Measurements of oil volume fraction and velocity distributions in vertical oil-in-water flows using ERT and a local probe. *Journal of Zhejiang University. Science*. 2005;**6A**(12):1412-1415

[24] Vigneaux P, Chenais P, Hulin JP. Liquid-liquid flows in an inclined pipe. *AIChE Journal*. 1988;**34**:781-789

[25] Flores J, Chen XT, Brill JP. Characteristics of oil-water flow patterns in vertical and deviated well. *SPE Production & Facilities*. 1999;**14**(2):94-101

Heat Transfer and Fluid Flow Investigations in PDMS Microchannel Heat Sinks Fabricated by Means of a Low-Cost 3D Printer

Inês Maia, Cesar Rocha, Pedro Pontes, Vanessa Cardoso, João M. Miranda, Ana S. Moita, G. Minas, António L.N. Moreira and Rui Lima

Abstract

Polydimethylsiloxane (PDMS), due to its remarkable properties such as optical transparency and ability to easily mold, is one of the most popular polymers used in micro- and nanofluidics. Furthermore, 3D printing technology due to its low cost and simplicity is also gaining a great interest among the microfluidic community. In this work, the potential of 3D printing is shown to produce microfluidic devices, their ability for studying flows and heat transfer of nanofluids, and their applicability as a heat sink device. The low-cost fused deposition modeling 3D printing technique was combined with a PDMS casting technique for the microfluidic device fabrication. The potential of this technique was experimentally demonstrated by fluid flow and heat transfer investigations using different fluids, such as distilled water-, alumina (Al_2O_3)-, and iron oxide (Fe_3O_4)-based nanofluids. The simplicity, low-cost, and unique features of the proposed heat sink device may provide a promising way to investigate nanofluids' flow and heat transfer phenomena that are not possible to be studied by the current traditional systems.

Keywords: microfluidics, 3D printing, microchannel heat sinks, nanofluids, heat transfer, electronics cooling

1. Introduction

The continuous investigation on strategies for size reduction while maintaining, or even increasing, power of technological devices demands cooling systems with higher thermal efficiency and smaller sizes. One approach relied on the modification of heat sinks by incorporating microchannels to increase the heat exchange surface. Despite being a well-adopted strategy, its complex configurations proved to be difficult to manufacture [1, 2]. Other strategies focused on the type of the used fluids for the cooling process. Dielectric fluids [1, 3], two-phase fluids [3, 4], and nanofluids (NFs) [5–8] have been thoroughly investigated. Among these three,

the nanofluids, which are fluids comprised of particles, with size ranging from 1 to 100 nm, suspended in a base fluid, have been reported as presenting a better thermal conductivity than the base fluid [8, 9]. Nevertheless, some challenges regarding their usage, such as agglomeration, long-term stability, and high-costs, still need further investigation [8, 10–12]. The most commonly used nanoparticles (NPs) for NFs are metallic, such as Cu, Ag, Au, and Fe, or non-metallic such as Al_2O_3 , CuO, TiO_2 , SiC, and carbon nanotubes. Many authors reported that the heat transfer of NFs is influenced by several factors such as shape, dimensions, volume fractions in the suspensions, and the thermal properties of the particle materials [11, 13, 14]. Therefore, enhancement in heat transfer was also reported, but only for small concentrations of NPs [8, 9].

Abareshi et al. [15] have evaluated the thermal conductivity of nanofluids with different volume fractions of Fe_3O_4 NPs, at different temperatures. The thermal conductivity was reported to increase up to 11.5% for a volume fraction of 3 vol% at 40°C. Xia et al. [16] have investigated the heat transfer coefficient of nanofluids using TiO_2 and Al_2O_3 NPs, with different volume fractions. For a volume fraction of 1%, the heat transfer coefficient was significantly increased for both nanofluids, compared with deionized water. Gavili et al. [17] have studied the thermal conductivity of ferrofluids with Fe_3O_4 particles of approximately 10 nm in diameter, suspended in deionized water. With the application of a magnetic field, the thermal conductivity was increased up to 200% for a 5% volume fraction. Kim et al. [18] have investigated the thermal conductivity of alumina- and distilled water-based nanofluids, with concentrations of 0.5, 1, and 2 wt%. The conductivity was found to increase with the increasing of the NPs concentration. Al-Rjoub et al. [19] have tested four cooling liquids: deionized water; distilled water; borax buffer; and Al_2O_3 NPs solution, on a microscale heat exchanger. It was found that the deionized water has presented the lowest heat removal capacity, while the Al_2O_3 solution showed the highest capacity, corresponding to about 69% increase.

The majority of microchannel heat sink devices that can be found in literature were fabricated in silicon, due to its thermal conductivity. However, the fabrication process of those devices can be laborious and needs extremely expensive facilities. Novel, fast, and low-cost fabrication techniques have been developed by means of different kinds of polymers [20–22]. PDMS is a silicone elastomer with a set of properties that make it suitable for many applications and is a popular choice for microfluidic devices fabrication [21, 22]. Besides being cheaper than the monocrystalline silicon, it presents a low elasticity change versus temperature, high thermal stability, chemical inertness, dielectric stability, shear stability, high compressibility, and hyperelasticity [23–27]. Moreover, it is non-toxic and biocompatible [25, 27–29]. PDMS devices can be manufactured by simple techniques at room temperature, such as replica molding.

The 3D printers are gaining an increased attention by both academic and industrial community to produce microdevices and models at an extremely low cost. Some successful applications can already be found in lab-on-a-chip tools [30], microfluidics [31, 32], and biomedical *in vitro* devices [27, 32–34]. There are different kinds of printing methods such as the Fused Deposition Modeling (FDM) and stereolithography [32]. Among those methods, the most popular, simple method with the lowest cost is the FDM technology [32]. For this reason, the FDM process was combined with a PDMS casting technique to produce a PDMS microfluidic device. Hence, the main objective of this work is to show the potential of a FDM 3D printer to produce microfluidic devices and their potential to be used to perform flows and heat transfer studies of nanofluids. To demonstrate the potential of this technique, fluid flow and heat transfer studies were performed by using different fluids such as distilled water-, alumina (Al_2O_3)-, and iron oxide (Fe_3O_4)-based nanofluids with concentrations of 1 and 2.5%.

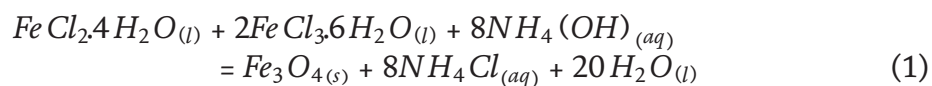
2. Materials and methods

This section describes the experimental protocol to develop the nanofluids and the fabrication process to produce the heat sinks, as well as the used experimental setup.

2.1 Nanoparticles preparation

Two different types of NPs were used on the flow and heat experiments: alumina oxide (Al_2O_3) NPs acquired from Sigma Aldrich (ref. 702,129, Sigma Aldrich) and iron oxide (Fe_3O_4) NPs synthesized on our laboratory by co-precipitation. This last method allows to produce magnetic iron oxide NPs in a cost-effective way and is appropriate for mass production. The Al_2O_3 NPs had a size inferior to 50 nm, while the synthesized Fe_3O_4 NPs had an average size of 11 ± 2 nm.

The co-precipitation was initiated with the preparation of the precipitation agent by adding 0.01 g of cetrimonium bromide (CTAB), diluted in 3 mL of distilled water, to 20 mL of ammonium hydroxide (NH_4OH). Hereinafter, a ferrous solution was prepared by diluting 7.78 g of iron(III) chloride ($FeCl_3$) and 4.06 g of iron(II) chloride ($FeCl_2$) in 20 mL of distilled water, in an ultrasonic bath. The solution was subsequently mechanically stirred at, approximately, 1500 rpm. The precipitation solution was then added, dropwise, to the ferrous solution under stirring, on a laminar flow cabinet. The co-precipitation occurred according to the following equation:



To conclude the process, the NPs were washed several times with distilled water with the assistance of a strong magnet.

Figure 1 shows the synthesized NPs and the representative transmission electron microscopy (TEM) image. A detailed description of this process can be found at Cardoso et al. [35].

Despite the TEM images show the aggregates of Fe_3O_4 NPs, in the NF, they were stable and non-aggregated for a period of time after 10 min of ultrasonic bath.

The NPs show a normalized magnetization of ~ 69 emu.g⁻¹ at ~ 10 kOe, which corresponds to the saturation magnetization, and also show a superparamagnetic behavior with an extremely low coercivity of 1.6 Oe [35–37].

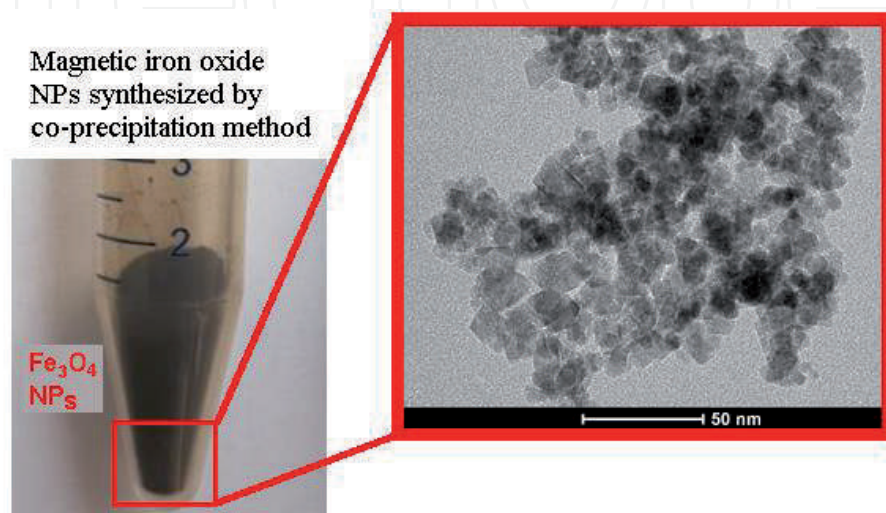


Figure 1. Magnetic iron oxide NPs and representative TEM image, adapted from [35, 36].

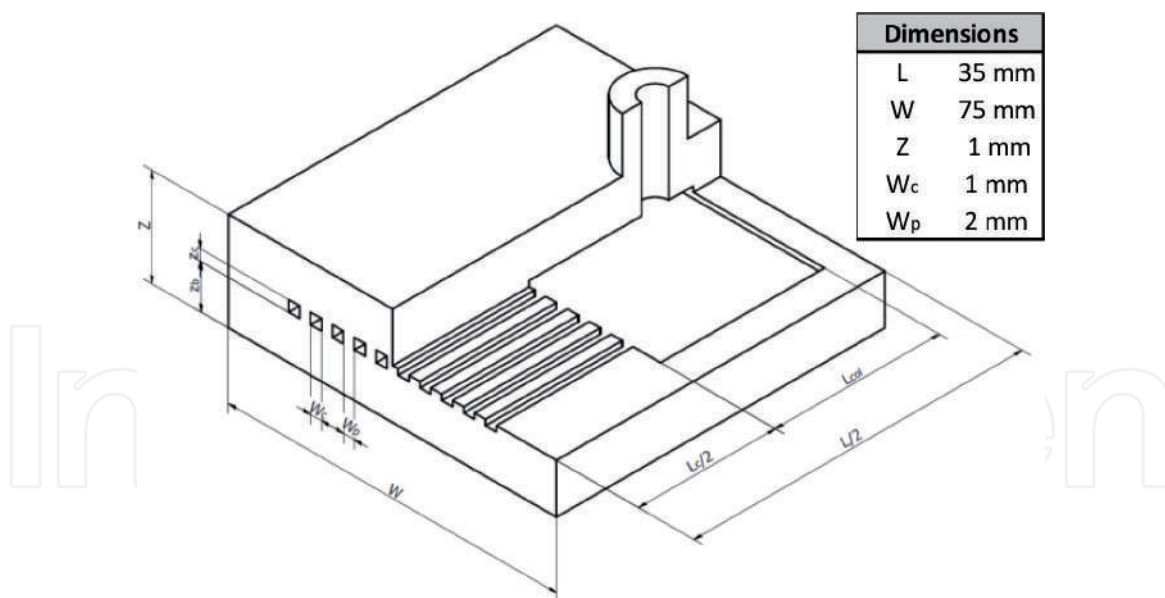


Figure 2.
Schematic representation of the main dimensions of the ABS master mold.

2.2 Fabrication of the heat sink microchannel

The heat sink microchannel device was produced based on a scaffold-removal technique [25]. First, the molds were drawn by using the Autodesk Inventor® software and then printed at the FDM 3D printer Ultimaker 2+ (Ultimaker, Netherlands). The first mold was printed with acrylonitrile butadiene styrene (ABS), whereas the second one was printed with polylactic acid (PLA). The fabrication of the molds was performed with a nozzle with a diameter of 0.4 mm, whereas the layer resolution was about 100 μm . The main dimensions of the ABS master mold can be found in **Figure 2**.

Once the 3D models were printed, PDMS was prepared by adding a PDMS curing agent into the pre-polymer with a mixing ratio of 1:10. The PDMS was poured onto the PLA mold with the ABS master mold inside it. Once the PLA mold was filled with PDMS, the elastomer was cured at room temperature for about 1 day. Finally, the PDMS was removed from the PLA mold and immersed in an acetone bath to remove the ABS for approximately 24 h. **Figure 3** shows the schematic diagram of all the main steps to produce the PDMS heat sink device. The overall cost to fabricate the PDMS heat sink device is about 3.8 €. This cost includes the printing of the ABS master mold (~ 1 €) and PDMS casting process (~ 2.8 €).

Notice that after the PDMS curing process, small holes were made below the inlet and outlet to insert the thermocouples (type K). **Figure 4** shows the PDMS heat sink microfluidic device used in the flow and heat experiments.

2.3 Experimental procedures

The PDMS heat sink was placed on top of a hot plate controlled by a 9400-temperature controller (CAL Controls). The temperature of the plate was set to 60°C, whereas the flow rate of the fluids was controlled by a syringe pump (Harvard) connected to the inlet of the heat sink. The temperature at the entrance and exit of the device was acquired through a data acquisition instrument connected to the thermocouples of the device. Wood and polystyrene blocks were used to minimize the heat losses. **Figure 5** shows a schematic diagram of the experimental setup. The flow of the Fe_3O_4 nanofluid was analyzed by optical microscopy at a flow rate of 10 $\mu\text{L}/\text{min}$. Note that the temperature measurements presented

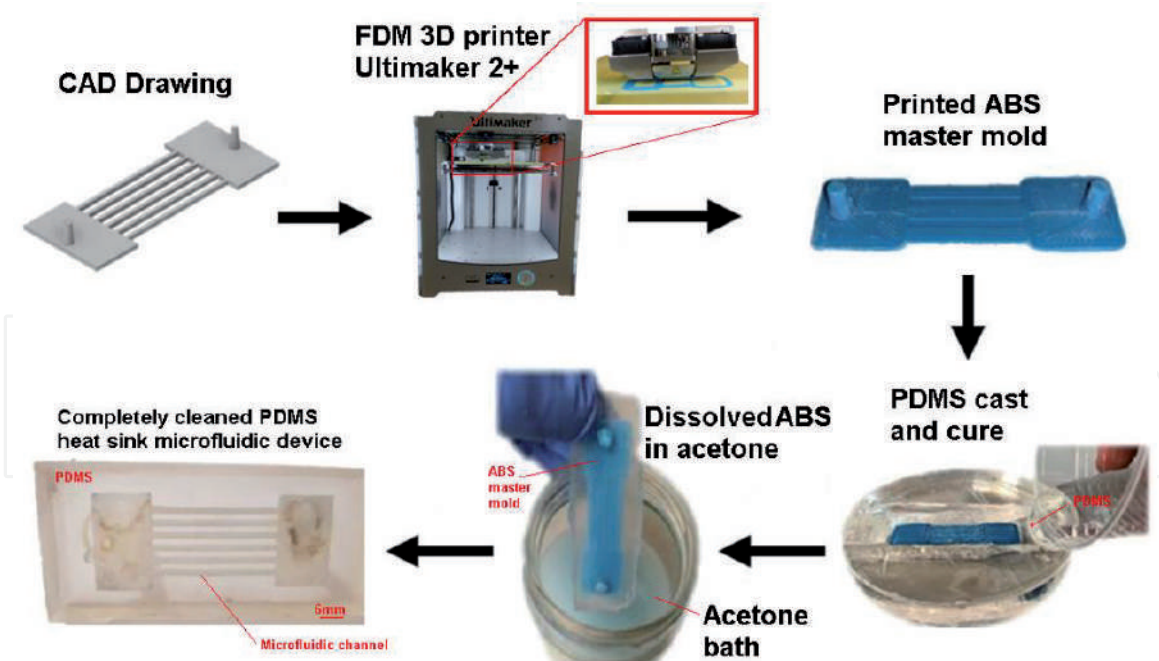


Figure 3.
 Schematic representation of main steps to fabricate the PDMS heat sink.

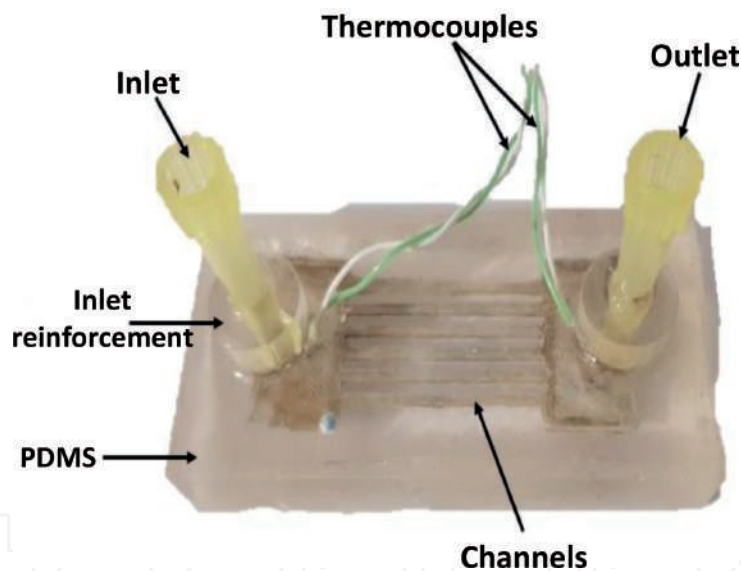


Figure 4.
 PDMS heat sink microfluidic device with the inserted thermocouples.

an uncertainty of $\pm 1^\circ\text{C}$. The thermographic studies were performed with distilled water at a flow rate of 1, 5, 7.5, 10, and 15 mL/min and a thermographic camera Onca-MWIR-InSb (Xenics Infrared Solutions). The setup and calibration procedures of the camera were performed as in Teodori et al. [38]. Images, with a resolution of $150\text{px} \times 150\text{px}$, were taken with a frame rate of 1000 fps.

To evaluate the influence of the nanofluids properties in the heat sink microfluidic device, the tests were performed using distilled water, Fe_3O_4 at a concentration of 1 and 2.5%, and Al_2O_3 at the same concentrations. All the fluids were set to a flow rate of 1 up to 30 mL/min.

2.4 Heat transfer calculations

The properties of the nanofluids were obtained taken into account fundamental equations described on previous studies [39, 40]. The thermal conductivity of the

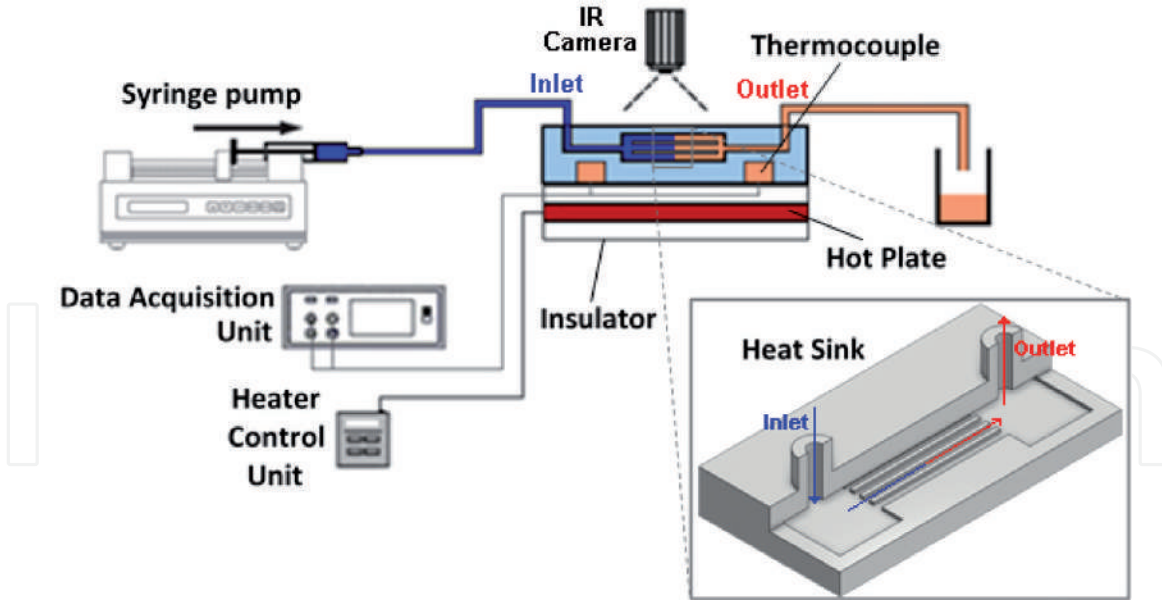


Figure 5.
Schematic representation of the experimental setup.

nanofluid was obtained according to the Maxwell model described by the following Equation [39, 40]:

$$K_{nf} = K_{bf} \left(\frac{K_p + 2K_{bf} + 2\phi(K_p - K_{bf})}{K_p + 2K_{bf} - 2\phi(K_p - K_{bf})} \right), \quad (2)$$

where K_{nf} is the nanofluid thermal conductivity, K_p is the NPs thermal conductivity, K_{bf} is the base fluid thermal conductivity, and ϕ is the NPs concentration.

The nanofluid density and heat capacity were calculated through the weighted average of the individual properties of both the NPs and base fluid. The first is expressed by Eq. (3) [14, 41] and the latter by Eq. (4) [11, 14].

$$\rho_{nf} = \rho_p \phi + \rho_{bf}(1 - \phi), \quad (3)$$

$$c_{p_{nf}} = \phi \rho_p c_{p_{np}} + (1 - \phi) \rho_{fb} c_{p_{bf}} \quad (4)$$

In the abovementioned equations, ρ_{nf} represents the nanofluid density, ρ_p the particle density, ρ_{bf} the base fluid density, and $c_{p_{np}}$ and $c_{p_{bf}}$ the specific heat capacity of the NPs and of the base fluid, respectively.

The nanofluid viscosity was determined through the equation proposed by Batchelor [42]:

$$\mu_{nf} = (1 + 2.5\phi + 6.2\phi^2) \mu_{fb}, \quad 0 < \phi < 10\% \quad [5]$$

where μ_{nf} is the nanofluid viscosity and μ_{fb} the base fluid viscosity. This equation brings in a quadratic dependence with the volume fraction, which provides a better representation of the interaction between the particles on the fluid.

Within the microfluidic device, the heat transfer will occur by convection inside the microchannels and by conduction in the walls between them. Consequently, the mathematical approach that better allowed the evaluation of the heat transfer was described by Ma et al. [10]. The convection heat transfer coefficient was calculated by iterations using the following equations:

$$h = \frac{Q}{N(A_b + 2\eta A_i)(T_b - T_{avgf})}, \quad (5)$$

$$m_i = \sqrt{\frac{2h_{i-1}}{k_{PDMS}w_p}}, \quad (6)$$

$$\eta_i = \frac{th(m_i z_c)}{m_i z_c}, \quad (7)$$

where A_b represents the area of microchannel bottom, A_l the area of microchannel sidewall, T_{avgf} the average temperature of the fluid, η the fin efficiency, w_p the average width of fin, and z_c the height of the channel. The main dimensions of the heat sink are illustrated in **Figure 2**. The heat transfer rate, Q , represents the amount of heat energy taken by the fluid when it flows through the channels and is given by Eq. (9). This parameter was obtained for each mass flow rate, \dot{m} , after the temperature at the inlet, T_{in} , and at the outlet, T_{out} , were measured.

$$Q = q \rho_f c_{pf} (T_{out} - T_{in}), \quad (8)$$

where q , c_{pf} and ρ_f is the volume flow rate, specific heat capacity, and density of the working fluid, respectively.

3. Results and discussion

In this section, the obtained results are presented and discussed. The temperature measurements and the known properties of the materials were used to calculate the parameters described on the previous section. Using those parameters, the influence of the environment conditions and of the fluid properties in heat transfer was analyzed.

3.1 Influence of the nanofluid properties

As described previously, the prepared nanofluids with iron oxide (Fe_3O_4) and alumina (Al_2O_3) NPs were used to verify the thermal properties influence of the nanofluids in the heat transfer performance of the developed PDMS heat sink device.

Figure 6 shows the temperature difference between the inlet and the outlet as the tested nanofluids flow through the proposed PDMS heat sink. Overall, it is possible to conclude that both tested nanofluids present a bigger temperature difference between the inlet and the outlet in comparison with distilled water. Hence, these measurements indicate that the amount of heat energy absorbed by both nanofluids was bigger than that absorbed by the distilled water. In addition, the amount of heat absorbed by the nanofluids was found to be bigger for smaller flow rates, as shown in **Figure 6**. These results corroborate the measurements performed by Chein and Chuang [43], where they have investigated the heat performance of nanofluids with CuO NPs in a microchannel heat sink. These results also show that the flow rate affects the amount of heat absorbed by the nanofluids.

In **Figure 7**, an increase of the convective heat transfer coefficient was registered on both nanofluids, in comparison to the base fluid. The increase was more pronounced for the alumina nanofluid due to the greater stability of the nanofluid and bigger thermal conductivity of these kind of NPs [6]. By increasing the convective heat transfer coefficient, an increase of the heat transfer rate is expected. In **Figure 8**, it is possible to observe an increase in the heat transfer rate for both tested nanofluids in comparison with distilled water. From these results, it is also possible to conclude that for both nanofluids, the convective heat transfer coefficient and heat transfer rate increase with the flow rate, which agrees with the results obtained by Wen and Ding [44].

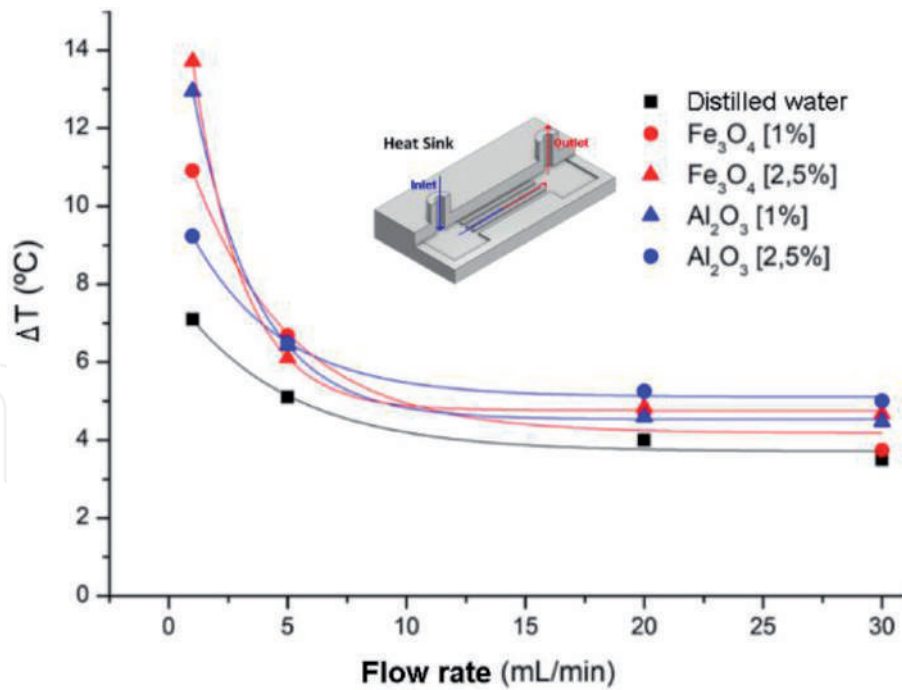


Figure 6. Temperature difference between the inlet and the outlet for the tested nanofluids at the proposed PDMS heat sink microfluidic device.

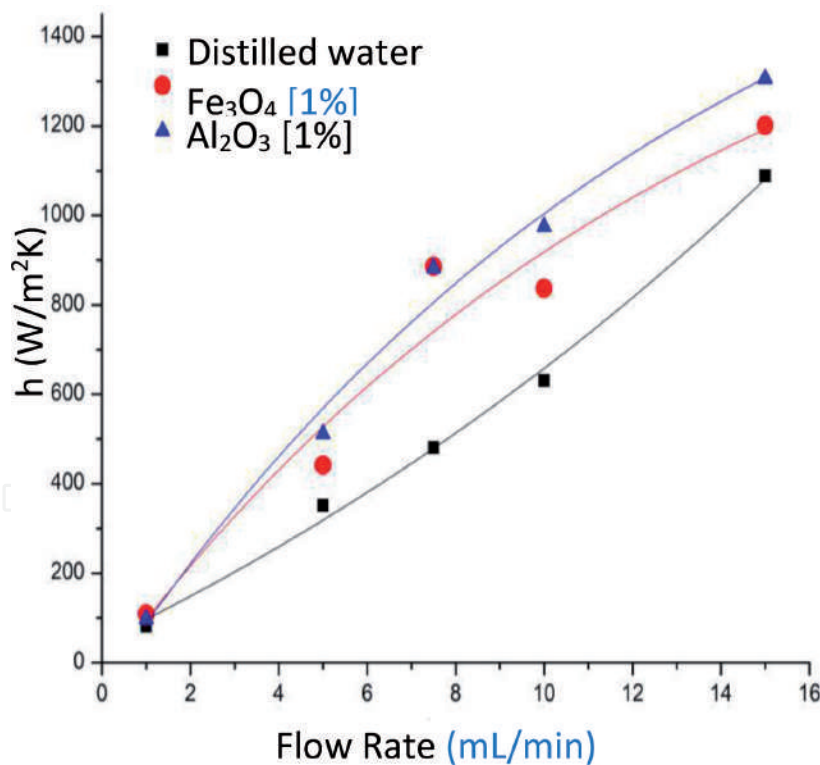


Figure 7. Convective heat transfer coefficient of distilled water, alumina, and iron oxide nanofluids as the function of the flow rate.

Figure 9 compares the convective heat transfer coefficient for two different concentrations of NPs, i.e., 1 and 2.5% of both Fe_3O_4 and Al_2O_3 . From a macroscopic view, it was noted a better dispersion for the nanofluids containing 1% of NPs. In addition, by increasing the concentration, the heat transfer was not enhanced. In fact, it was noted a decrease of the convective heat transfer coefficient when the concentration of NPs was increased to 2.5%. Although these results are somewhat

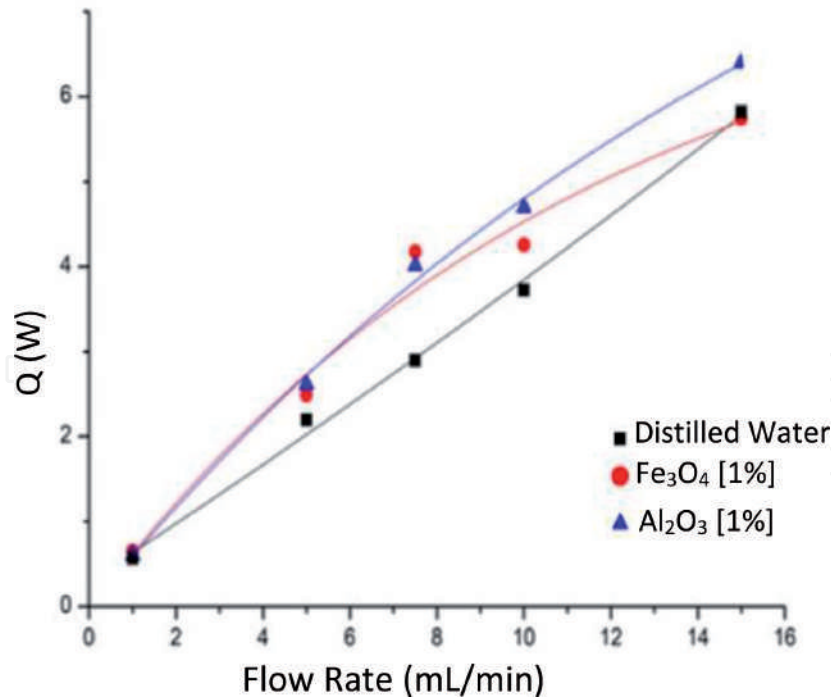


Figure 8. Heat transfer rate of distilled water, alumina, and iron oxide nanofluids as the function of the flow rate.

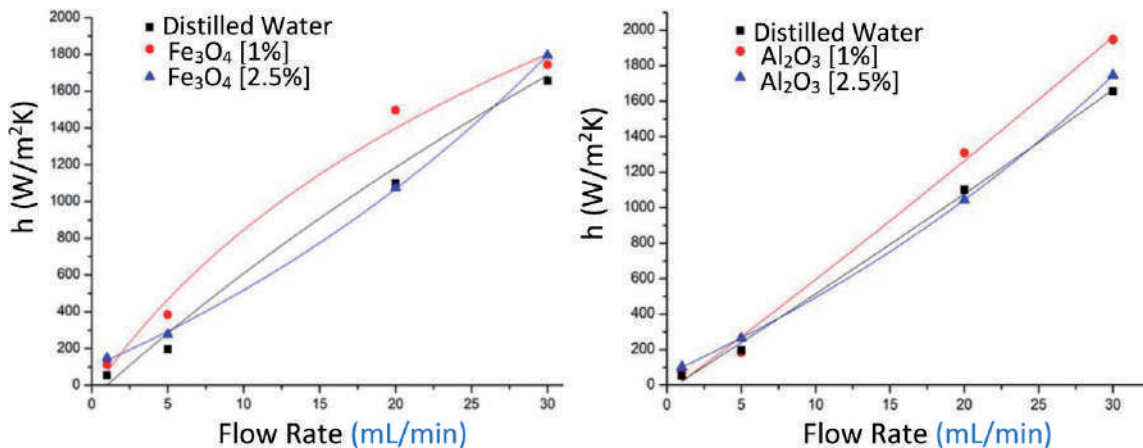


Figure 9. Convective heat transfer coefficient of nanofluids as the function of the flow rate, for two different concentrations of alumina and iron oxide NPs.

paradoxical, other researchers, such as Wen and Ding [45] and Putra et al. [46], have reported similar results. The main possible reasons for the seen heat transfer deterioration include both the aggregation and sedimentation of the NPs. However, the possible reasons and mechanism attributed to such phenomena require further research. Currently, our group is carrying out both experimental and numerical work to identify the exact causes for such phenomena.

3.2 Optical and thermal imaging analyses

The biggest advantage of the developed PDMS heat sink device is the ability to visualize the flow phenomena happening inside the microchannels. By using a high-speed video microscopy system, it was possible to visualize several flow phenomena of the nanofluids such as the formation, growing, and breakdown of NPs clusters (see **Figure 10**). From these observations, it was concluded that one of the main causes for the formation of the clusters was the high roughness of the PDMS surface

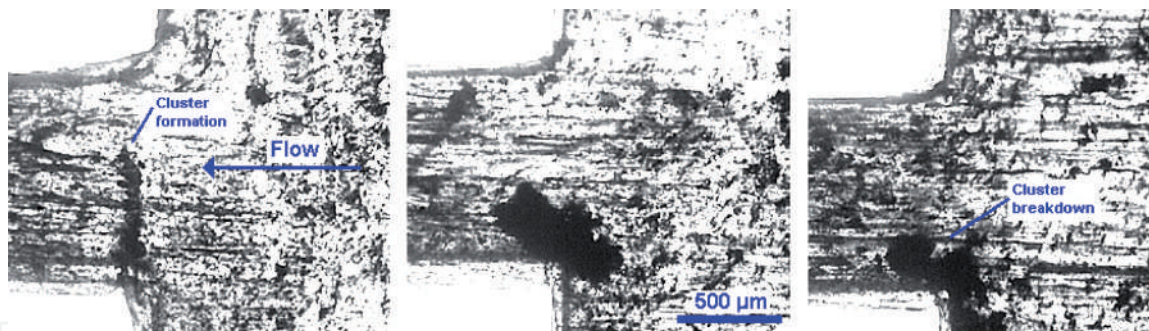


Figure 10.
Optical images of the formation, growing, and breakdown of a cluster of NPs.

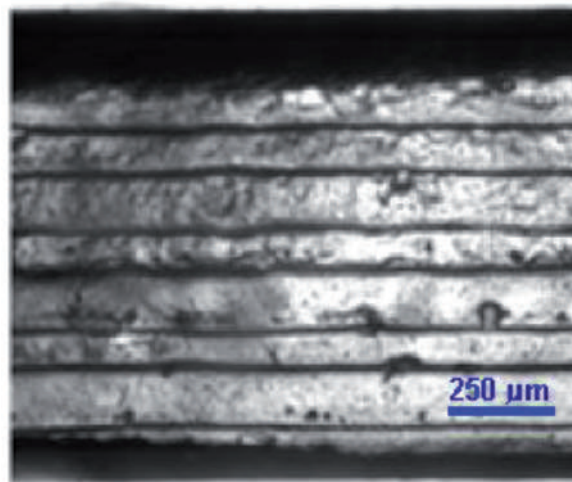


Figure 11.
Optical image of the surface roughness of the heat sink device used in this study.

channels (**Figure 11**). This verified roughness was caused by the ABS master mold fabricated by the FDM 3D printer. In order to improve the surface roughness, the ABS master molds should undergo an acetone vapor treatment before performing the PDMS casting procedure. More detailed information about this method can be found elsewhere [27].

Another interesting advantage of this PDMS microfluidic device is the ability to visualize both the flow and thermal performance of the system by using a thermographic camera, as shown in **Figure 12**. Notice that the temperatures acquired were from the surface of the heat sink device and not directly from the working fluid flowing in the microchannels. In fact, PDMS is transparent to visible radiation but partially opaque to the infrared (IR) radiation. Hence, to obtain the temperatures more closely related to the working fluids flowing through the microchannels, the thickness of the upper walls should be reduced in future experiments. A very interesting observation was the ability to detect bubbles that are likely to happen in microfluidic devices. In **Figure 13**, it is possible to visualize a bubble within the microchannel and the thermal performance of the heat sink device.

3.3 Limitations and future directions

In this study, a microchannel device was successfully manufactured and used in microfluidic essays. Nevertheless, some limitations arose throughout the work. Despite the advantages of using PDMS, some properties of the material, such as

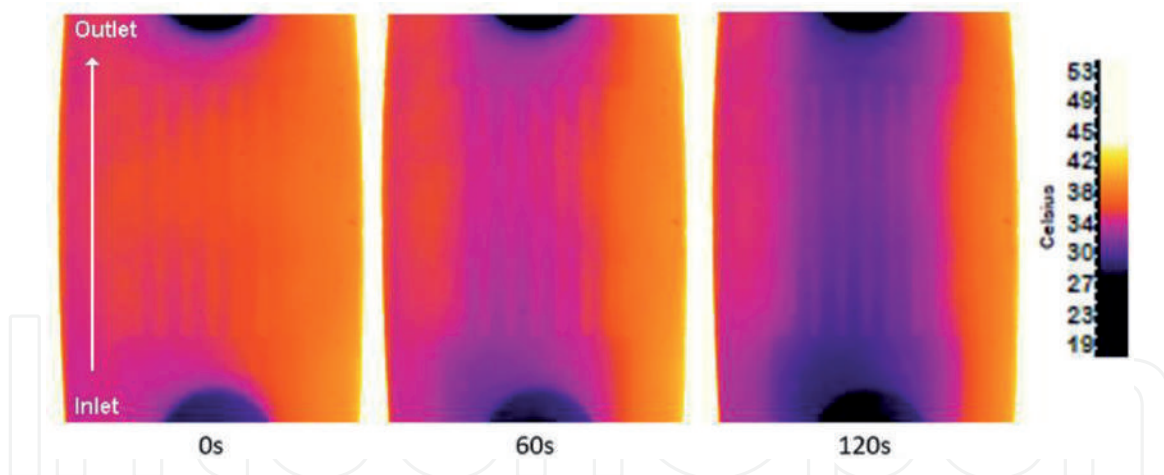


Figure 12.
Temperature gradient analyzed through the thermographic camera at three different instants: $t = 0$ s; $t = 60$ s, and $t = 120$ s.

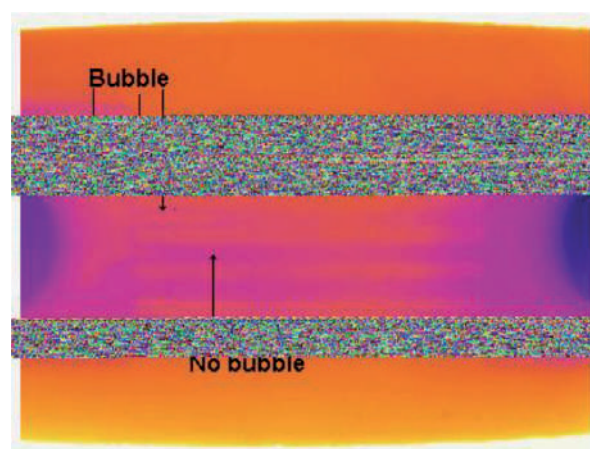


Figure 13.
Formation of a bubble at the entrance of the microchannels, which affects the thermal performance of the microfluidic device.

the low conductivity and partial opacity to the infrared (IR) radiation, were not favorable for the experiments. Also, the walls of the heat sink were rough due to the ABS master mold used in the fabrication technique, and the thickness should be reduced. The stability of the nanofluids has yet to be optimized since the deposition of NPs was detected on the heat sink walls. Future works will aim to improve of those limitations.

4. Conclusion

The main objective of this work was to show the potential of a PDMS heat sink microfluidic device to perform flows and heat transfer studies of nanofluids. The PDMS heat sink device was produced by using the FDM 3D printing process, combined with a PDMS casting technique. This fabrication process allowed to manufacture devices in an easy, low-cost, and reasonable reproductively way. To demonstrate the potential of the produced PDMS heat sink device, fluid flow and heat transfer studies were performed by using two different nanofluids, i.e., alumina (Al_2O_3)- and iron oxide (Fe_3O_4)-based nanofluids with concentrations of 1 and 2.5%. Overall, it was found that the thermal performance of the working nanofluids

is in good agreement with several past studies. For instance, it was noted that the heat energy absorbed by both nanofluids was higher than that absorbed by the distilled water. In addition, it was found that the flow rate affects the amount of heat absorbed by the nanofluids. However, the most interesting and unique results were the optical and thermal imaging results. These results were only possible due to the optical transparency of the PDMS heat sink device. Hence, by using this device, it was possible to visualize several flow phenomena of the nanofluids such as the formation, growing, and breakdown of NPs clusters. From these latter observations, it was possible to conclude that one of the main causes for the formation of the clusters was the high roughness of the PDMS surface channels caused by the surface roughness of the ABS master mold fabricated by the FDM 3D printer. This drawback can be overcome by performing an acetone vapor treatment before performing the PDMS casting. Overall, the simplicity, low-cost, and unique features of the proposed PDMS heat sink microfluidic device may prove a viable alternative tool to investigate nanofluids flow and heat transfer phenomena that are not possible to be performed by the current traditional systems.

Acknowledgements

This work was supported by *Fundação para a Ciência e a Tecnologia* (FCT) under the strategic grants UID/EMS/04077/2019, UID/EEA/04436/2019, and UID/EMS/00532/2019. The authors are also grateful for the funding of FCT through the projects POCI-01-0145-FEDER-016861, POCI-01-0145-FEDER-028159, NORTE-01-0145-FEDER-029394, and NORTE-01-0145-FEDER-030171, funded by COMPETE2020, NORTE2020, PORTUGAL2020, and FEDER. The authors also acknowledge FCT for partially financing the research under the framework of the project UTAP-EXPL/CTE/0064/2017, financiado no âmbito do Projeto 5665-Parcerias Internacionais de Ciência e Tecnologia, UT Austin Programme. Ana S. Moita also acknowledges FCT for her contract in the context of the recruitment programme FCT Investigator (IF/00810/2015) and exploratory project associated with it.

Conflict of interest

The authors declare no conflict of interest.

Nomenclature

A	area
cp	heat capacity
h	convection heat transfer coefficient
K	thermal conductivity
N	number of microchannels
q	volume flow rate
Q	heat rate
R	resistance
R _t	thermic resistance
T	temperature
wp	average width of fin
zc	height of the channel

Greek symbols

η	fin efficiency
μ	viscosity
φ	nanoparticle concentration
ρ	density

Subscript

b	microchannel bottom
bf	base fluid
ext.	exterior
f	fluid
in	inlet
l	microchannel sidewall
nf	nanofluid
out	outlet
p	nanoparticles

Author details

Inês Maia¹, Cesar Rocha², Pedro Pontes¹, Vanessa Cardoso³, João M. Miranda⁴, Ana S. Moita¹, G. Minas³, António L.N. Moreira¹ and Rui Lima^{2,4*}

¹ IN+ Center for Innovation, Technology and Policy Research, Instituto Superior Técnico, Universidade de Lisboa, Lisboa, Portugal

² MEtRICs, Mechanical Engineering Department, University of Minho, Guimarães, Portugal

³ CMEMS-UMinho, University of Minho, Guimarães, Portugal

⁴ CEFT, Faculdade de Engenharia da Universidade do Porto (FEUP), Porto, Portugal

*Address all correspondence to: rl@dem.uminho.pt

IntechOpen

© 2020 The Author(s). Licensee IntechOpen. This chapter is distributed under the terms Commons Attribution - NonCommercial 4.0 License (<https://creativecommons.org/licenses/by-nc/4.0/>), which permits use, distribution and reproduction for non-commercial purposes, provided the original is properly cited. 

References

- [1] Moura M, Teodori E, Moita AS, Moreira ALN. 2 phase microprocessor cooling system with controlled pool boiling of dielectrics over micro-and-nano structured integrated heat spreaders. In: 15th IEEE Intersociety Conference on Thermal and Thermomechanical Phenomena in Electronic Systems (ITherm). 2016. pp. 378-387
- [2] Abreu VT B e. Test and optimization of a two-phase thermosyphon cooling system for microprocessors under real working conditions. Instituto Superior Técnico; 2017
- [3] Abreu V, Harrison M, Gess J, Moita AS. Two-phase thermosyphon cooling using integrated heat spreaders with copper microstructures. In: Proc 17th Intersoc Conf Therm Thermomechanical Phenom Electron Syst ITherm 2018. 2018. pp. 645-652
- [4] Lameiras MM. Development of a Custom Made Condenser for a Two-Phase Thermosyphon CPU Cooling System. Instituto Superior Técnico; 2018
- [5] Cahill DG, Braun PV, Chen G, Clarke DR, Fan S, Goodson KE, et al. Nanoscale thermal transport. II. 2003-2012. Applied Physics Reviews. 2014;**1**(1):11305-5-11305-6. Available from: <http://aip.scitation.org/doi/10.1063/1.4832615>
- [6] Lomascolo M, Colangelo G, Milanese M, De Risi A. Review of heat transfer in nanofluids: Conductive, convective and radiative experimental results. Renewable and Sustainable Energy Reviews. 2015;**43**:1182-1198. DOI: 10.1016/j.rser.2014.11.086
- [7] Godson L, Raja B, Mohan Lal D, Wongwises S. Enhancement of heat transfer using nanofluids—An overview. Renewable and Sustainable Energy Reviews. 2010;**14**(2):629-641
- [8] Saidur R, Leong KY, Mohammad HA. A review on applications and challenges of nanofluids. Renewable and Sustainable Energy Reviews. 2011;**15**(3):1646-1668. DOI: 10.1016/j.rser.2010.11.035
- [9] Philip J, Shima PD. Thermal properties of nanofluids. Advances in Colloid and Interface Science. 2012;**183-184**:30-45
- [10] Ma DD, Xia GD, Wang J, Yang YC, Jia YT, Zong LX. An experimental study on hydrothermal performance of microchannel heat sinks with 4-ports and offset zigzag channels. Energy Conversion and Management. 2017;**152**:157-165
- [11] Xuan Y, Roetzel W. Conceptions for heat transfer correlation of nanofluids. International Journal of Heat and Mass Transfer. 2000;**43**(19):3701-3707
- [12] Philip J, Shima PD, Raj B. Evidence for enhanced thermal conduction through percolating structures in nanofluids. Nanotechnology [Internet]. 30 Jul 2008;**19**(30):305706 (7pp). Available from: <http://stacks.iop.org/0957-4484/19/i=30/a=305706?key=crossref.3d918427472835fc73f454942400dcac>
- [13] Zhu H, Zhang C, Liu S, Tang Y, Yin Y. Effects of nanoparticle clustering and alignment on thermal conductivities of Fe₃O₄ aqueous nanofluids. Applied Physics Letters. 2006;**89**(2):4-7
- [14] Pang C, Lee JW, Kang YT. Review on combined heat and mass transfer characteristics in nanofluids. International Journal of Thermal Sciences. 2015;**87**:49-67. DOI: 10.1016/j.ijthermalsci.2014.07.017
- [15] Abareshi M, Goharshadi EK, Mojtaba Zebarjad S, Khandan Fadafan H, Youssefi A. Fabrication, characterization

and measurement of thermal conductivity of Fe_3O_4 nanofluids. *Journal of Magnetism and Magnetic Materials*. 2010;**322**(24):3895-3901. DOI: 10.1016/j.jmmm.2010.08.016

[16] Xia GD, Liu R, Wang J, Du M. The characteristics of convective heat transfer in microchannel heat sinks using Al_2O_3 and TiO_2 nanofluids. *International Communications in Heat and Mass Transfer*. 2016;**76**:256-264

[17] Gavili A, Zabihi F, Isfahani TD, Sabbaghzadeh J. The thermal conductivity of water base ferrofluids under magnetic field. *Experimental Thermal and Fluid Science*. 2012;**41**:94-98. DOI: 10.1016/j.expthermflusci.2012.03.016

[18] Kim S, Tserengombo B, Choi SH, Noh J, Huh S, Choi B, et al. Experimental investigation of heat transfer coefficient with Al_2O_3 nanofluid in small diameter tubes. *Applied Thermal Engineering*. 2019;**146**:346-355. DOI: 10.1016/j.applthermaleng.2018.10.001

[19] Al-Rjoub MF, Roy AK, Ganguli S, Banerjee RK. Enhanced heat transfer in a micro-scale heat exchanger using nano-particle laden electro-osmotic flow. *International Communications in Heat and Mass Transfer*. 2015;**68**:228-235. DOI: 10.1016/j.icheatmasstransfer.2015.09.009

[20] Al-Rjoub MF, Roy AK, Ganguli S, Banerjee RK. Enhanced electro-osmotic flow pump for micro-scale heat exchangers. In: ASME 2012 Third International Conference on Micro/Nanoscale Heat and Mass Transfer [Internet]. American Society of Mechanical Engineers; 2012. pp. 829-833. Available from: <https://asmedigitalcollection.asme.org/MNHT/proceedings/MNHMT2012/54778/829/269200>

[21] Faustino V, Catarino SO, Lima R, Minas G. Biomedical microfluidic devices

by using low-cost fabrication techniques: A review. *Journal of Biomechanics*. 2016;**49**(11):2280-2292

[22] Catarino SO, Rodrigues RO, Pinho D, Minas G, Lima R. Blood cells separation and sorting techniques of passive microfluidic devices: From fabrication to applications. *Micromachines*. 2019;**10**:593. DOI: 10.3390/mi10090593

[23] Schneider F, Fellner T, Wilde J, Wallrabe U. Mechanical properties of silicones for MEMS. *Journal of Micromechanics and Microengineering*. 2008;**18**(6):065008 (9pp)

[24] Moreira NRP. Estudo de várias propriedades mecânicas do polidimetilsiloxano (PDMS) usado em dispositivos biomédicos. Instituto Politécnico de Bragança; 2013

[25] Saggiomo V, Velders AH. Simple 3D printed scaffold-removal method for the fabrication of intricate microfluidic devices. *Advancement of Science*. 2015;**2**(9):1500125

[26] Khanafer K, Duprey A, Schlicht M, Berguer R. Effects of strain rate, mixing ratio, and stress-strain definition on the mechanical behavior of the polydimethylsiloxane (PDMS) material as related to its biological applications. *Biomedical Microdevices*. 2009;**11**(2):503-508

[27] Pinho D, Bento D, Ribeiro J, Lima R, Vaz M. An In vitro experimental evaluation of the displacement field in an intracranial aneurysm model. In: Flores P, Viadero F, editors. *New Trends in Mechanism and Machine Science*. Cham: Springer International Publishing; 2015. pp. 261-268

[28] Mata A, Fleischman AJ, Roy S. Characterization of polydimethylsiloxane (PDMS) properties for biomedical micro/nanosystems. *Biomedical Microdevices*. 2005;**7**(4):281-293

- [29] Ainla A. Valves for microfluidic devices [Internet]. Chalmers University of Technology; 2007. Available from: http://www.ims.ut.ee/~alar/microtech/Ch1_4/Ch_1_4_4.php
- [30] Comina G, Suska A, Filippini D. 3D printed unibody lab-on-a-chip: Features survey and check-valves integration. *Micromachines*. 2015;**6**(4):437-451
- [31] Gaal G, Mendes M, de Almeida TP, Piazzetta MHO, Gobbi ÂL, Riul A, et al. Simplified fabrication of integrated microfluidic devices using fused deposition modeling 3D printing. *Sensors and Actuators B: Chemical*. 2017;**242**: 35-40. DOI: 10.1016/j.snb.2016.10.110
- [32] Faria CL, Pinho D, Santos J, Gonçalves LM, Lima R. Low cost 3D printed biomodels for biofluid mechanics applications. *Journal of Mechanical Engineering and Biomechanics*. 2018;**3**(1):1-7
- [33] Yap YL, Tan YSE, Tan HKJ, Peh ZK, Low XY, Yeong WY, et al. 3D printed bio-models for medical applications. *Rapid Prototyping Journal*. 2017;**23**(2):227-235
- [34] Souza A, Ribeiro J, Lima R. Manufacturing process of a brain aneurysm biomodel in PDMS using rapid prototyping. In: *Lecture Notes in Computational Vision and Biomechanics*. Berlin: Springer Nature; 2019
- [35] Cardoso VF, Irusta S, Navascues N, Lanceros-Mendez S. Comparative study of sol-gel methods for the facile synthesis of tailored magnetic silica spheres. *Materials Research Express*. 2016;**3**(7):1-7. DOI: 10.1088/2053-1591/3/7/075402
- [36] Lima R, Vega EJ, Cardoso VF, Minas G, Montanero JM. Magnetic PDMS microparticles for biomedical and energy applications. In: *Lecture Notes in Computational Vision and Biomechanics*. Berlin: Springer Nature; 2019
- [37] Cardoso VF, Miranda D, Botelho G, Minas G, Lanceros-Méndez S. Highly effective clean-up of magnetic nanoparticles using microfluidic technology. *Sensors and Actuators B: Chemical*. 2018;**255**:2384-2391. DOI: 10.1016/j.snb.2017.08.095
- [38] Teodori E, Pontes P, Moita AS, Moreira ALN. Thermographic analysis of interfacial heat transfer mechanisms on droplet/wall interactions with high temporal and spatial resolution. *Experimental Thermal and Fluid Science*. 2018;**96**:284-294. DOI: 10.1016/j.expthermflusci.2018.03.013
- [39] Lamas B, Abreu B, Fonseca A, Martins N, Oliveira M. Critical analysis of the thermal conductivity models for CNT based nanofluids. *International Journal of Thermal Sciences*. 2014;**78**:65-76. DOI: 10.1016/j.ijthermalsci.2013.11.017
- [40] Aybar H, Sharifpur M, Azizian MR, Mehrabi M, Meyer JP. A review of thermal conductivity models for nanofluids. *Heat Transfer Engineering*. 2015;**36**(13):1085-1110
- [41] Pak BC, Cho YI. Hydrodynamic and heat transfer study of dispersed fluids with submicron metallic oxide particles. *Experimental Heat Transfer*. 1998;**11**(2):151-170
- [42] Pavlik M. The dependence of suspension viscosity on particle size, shear rate, and solvent viscosity. 2009. Available from: <http://via.library.depaul.edu/etd/71>
- [43] Chein R, Chuang J. Experimental microchannel heat sink performance studies using nanofluids. *International Journal of Thermal Sciences*. 2007;**46**(1):57-66
- [44] Wen D, Ding Y. Experimental investigation into convective heat transfer of nanofluids at the entrance region under laminar flow conditions.

International Journal of Heat and Mass
Transfer. 2004;**47**(24):5181-5188

[45] Wen D, Ding Y. Formulation of
nanofluids for natural convective heat
transfer applications. International
Journal of Heat and Fluid Flow.
2005;**26**(6):855-864

[46] Putra N, Roetzel W, Das SK. Natural
convection of nano-fluids. Heat and
Mass Transfer. 2003;**39**(8-9):775-784

IntechOpen

The Characteristics and Application of Nanofluids in MQL and MQCL for Sustainable Cutting Processes

Tran The Long and Tran Minh Duc

Abstract

Recently, there has been growing attention to nanofluids, especially in industry. More and more people nowadays see nanoparticle applications in various fields such as automotive, agriculture, medicine, machining, and so on. The addition of different nanoparticles to fluids has shown enormous advantages, particularly for improving the efficiency and therefore lowering the energy consumption of processes for addressing a wide range of global challenges related with energy and environmental problems. Nanoparticles are of great scientific interest as they are in that nanofluid with unusual effects, and ultra-small sizes will be a new area for researchers and definitely offer novel mechanisms and technologies in the future. In this chapter, the authors will mainly present the characteristics as well as latest advances in applications of nanofluids in machining practices. Nanoparticle additives contribute to reduce friction coefficient, lower the energy consumption, and significantly extend tool life by lowering thermal stress, from which the surface quality of manufactured parts improves. Moreover, the nanoparticle application in some of the green technologies as MQL and MQCL using vegetable oils not only brings out superior cooling and lubricating properties and minimizes the use of cutting fluids, but also creates new solutions for machining, especially for difficult-to-cut materials.

Keywords: nanoparticles, nanofluid, sustainable cutting, MQL, MQCL, hard machining, vegetable oil, metal cutting

1. Introduction

Climate change has become the most growing concern of people around the world. The rapid increase of population consequently leads to the use of more natural resources and giving out of more waste. The pollution in air, water, and food causes many serious human diseases. Accordingly, environmental laws are continuously tightening up to protect our Earth. Being a part of the production chain, manufacturing engineers are demanded not only to produce the products to meet the growing demand for higher quality and productivity but also to be responsible for achieving the sustainability in manufacturing. In metal cutting industries, the used cutting fluids after using for cooling and lubricating the contact zone contribute the largest amount of disposal (around 30%), which finally ends up as the

contamination in the rivers leading to the water pollution [1]. Therefore, it is necessary to find the solutions to reduce or eliminate the usage of coolants. Over some last decades, there were numerous studies concerning the reduction of coolant usage in machining, and dry cutting processes, the truly environmental-friendly method, had drawn most attention and brought out the obvious cost benefits derived from the elimination and treatment of cutting fluids. However, the selection of the proper cutting tools or inserts plays a very important role to ensure the proper tool life and high precision and accuracy of machined parts [2], and it also causes a strong influence on technological and economic characteristics. Recently, to meet the continuously increasing demand for cutting difficult-to-cut materials having high-graded mechanical properties and high hardness, the tools with geometrically defined cutting edges are directly used for machining the heat-treated materials, with the typical hardness of 45–70 HRC [3]. These processes are called hard machining, which has become the research trend in mechanical applications due to high productivity and accuracy. Up to now, people have seen hard machining more in metal cutting field, and therefore many of traditional grinding processes have been replaced. The new approach not only provides the alternative solution for cutting hard materials but also improves the cutting performance, significantly reduces coolant usage, and has low machine tool investment. On the other hand, the thermal shock caused by the use of cutting fluids must be seriously considered to avoid the insert breakage, so the flood cooling is not usually used for hard machining processes, especially for interrupted cutting. Furthermore, the enormous heat and high forces arising from cutting zone are the most challenging problems of hard cutting processes, which always demand the appropriate uses of high-graded cutting tools like coated carbide, ceramic, polycrystalline cubic boron nitride (PCBN), and diamond inserts [2, 4, 5]. Accordingly, minimum quantity lubrication (MQL) technique was proposed and proven to use and exhibited the promising results in some last decades [1, 6, 7]. The cutting fluids in forms of oil mist are directly sprayed to cutting zone, so the lubricating effect is very high to decrease the friction coefficient, from which cutting forces, cutting temperature, and tool wear reduce significantly, and tool life is extended. Interestingly, the minimal use of cutting fluid makes MQL an environmental friendly technique, and the vegetable oils can be used for hard cutting, which contributes to protect environment [8]. The main drawback of MQL method is the low cooling effect, which limits the applicability and cutting performance of hard machining [9, 10]. In order to develop MQL technique, there have been many studies proposing the very promising solutions to enhance the cooling performance, which includes MQL using nanofluids, minimum quantity cooling lubrication (MQCL), and MQCL using nano additives. In this chapter, the authors mainly discuss the latest studies on those up-to-date techniques used in hard machining processes.

This chapter is divided into five sections. Section 1 of the chapter provides the literature review of new development of MQL and MQCL technology using nanofluids for sustainable cutting processes. Section 2 is dedicated to hard machining under MQL condition using nanofluid. Section 3 describes the application of MQCL condition based on the new approach for hard cutting processes. Section 4 contains the latest advances on the utilization of nano additives for improving MQCL hard machining performance. Finally, Section 5 draws out the conclusions and some suggestion for future work.

2. Hard machining under MQL condition using nanofluid

Using nano additives suspended in MQL based fluids has opened a new approach for machining difficult-to-cut materials and is also an up-to-date research

topic gaining the growing concerns, especially for encountering climate change. There are many types of nanoparticles, such as Al_2O_3 , MoS_2 , SiO_2 , ZrO_2 , CuO , TiO_2 , CNT, ND, and so on, proven to use for improving the tribological property, thermal conductivity, and viscosity [11].

2.1 The improvement of cutting performance

In order to apply this technique in machining practice, the parameters of MQL (the based fluid, air pressure, flow rate) and nanofluid (the type, size, and concentration of nanoparticles) are needed to study and optimize, because they have strong effects on the cutting process. If the inappropriate values of each parameter are chosen, the little effectiveness and even the negative influence may occur in machining responses.

Li et al. [12] investigated MQL grinding process for Ni-based alloy using six different types of nanofluids. The results indicated that the viscosity and thermal conductivity of nanofluids significantly improve when compared to the base fluids. The authors also pointed out that CNT nano additives exhibit the highest heat transfer coefficient. Hence, the cutting temperature and forces decrease. Another observation done by Ali et al. [13] indicated that the viscosity of Al_2O_3 and TiO_2 nano-lubricants increases while their kinematic viscosity decreases slightly. Through the experiments, the coefficient of friction, power consumption, and wear rate much reduced due to the rolling performance together with the formation of tribo-films created by Al_2O_3 nanoparticles. Moreover, the technical specification and concentration of nanoparticles play a very important role and strongly influence on the machining responses. For finish cutting, the nanoparticles with smaller grain size and higher concentration should be used to improve the surface quality and reduce the cutting forces [11]. Pashmforoush and his co-authors [14] reported that the big improvement in surface roughness in grinding process of Inconel 738 super alloy is about 62.16 and 36.36% compared to those of dry and flood conditions, respectively. The enhancement of lubricating effect was also reported in milling under MQL using MoS_2 nanofluid, from which the friction coefficient reduced to extend the tool life and improve the surface quality [15]. The presence of nanoparticles in MQL based fluid not only improves the cooling and lubricating effects but also brings out the better cutting performance for machining difficult-to-cut materials. Moreover, this approach will successfully replace the dry and flood conditions, which fulfill the technological, economic, and environmental requirements, suitable for modern manufacturing. The performance investigation of end milling of SKD 11 steel using HSS tools under nanofluid MQL was done in [16]. The experiments are set up and shown in **Figure 1**. The cutting condition includes the three values of cutting speeds of 18, 24, and 30 m/min, feed rate of 0.01 mm/tooth, and axial depth of cut of 3 mm. The diameter of end mill is 10 mm. Al_2O_3 nano additives (0.5 wt%) are enriched in emulsion and soybean-based oil.

Through experimental results, the cutting force components F_x , F_y , and F_z when changing the cutting speeds and based fluid are shown in **Figures 2–4**. Under NFMQL with emulsion-based oil, the cutting forces F_x , F_y , and F_z reduce with the increase of cutting speed from 18 to 30 m/min. At a cutting speed of 30 m/min, the comparison between emulsion and soybean oil is made to find out the effect of the based fluid on machining responses. It can be clearly seen that the cutting forces reduce due to the better lubricating performance of soybean oil compared to emulsion fluid.

In addition, the tool life under NFMQL using soybean oil much improves and is over two times longer than that under the case using emulsion fluid (**Figure 5**). The investigation of tool wear is shown in **Figures 6–8**. They clearly reveal that notch wear and flank wear on HSS end mills increase with the rise of cutting

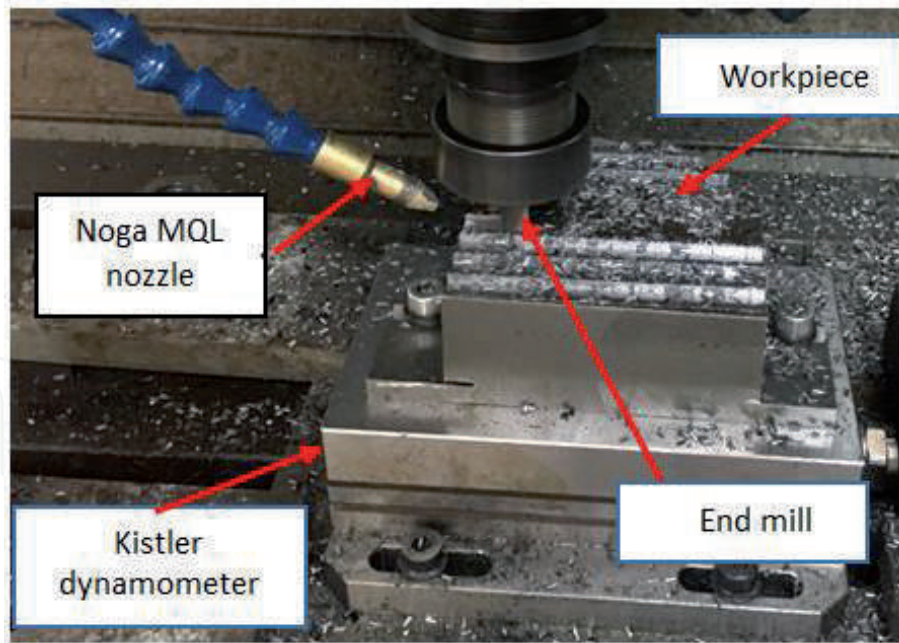


Figure 1.
Experimental setup [16].

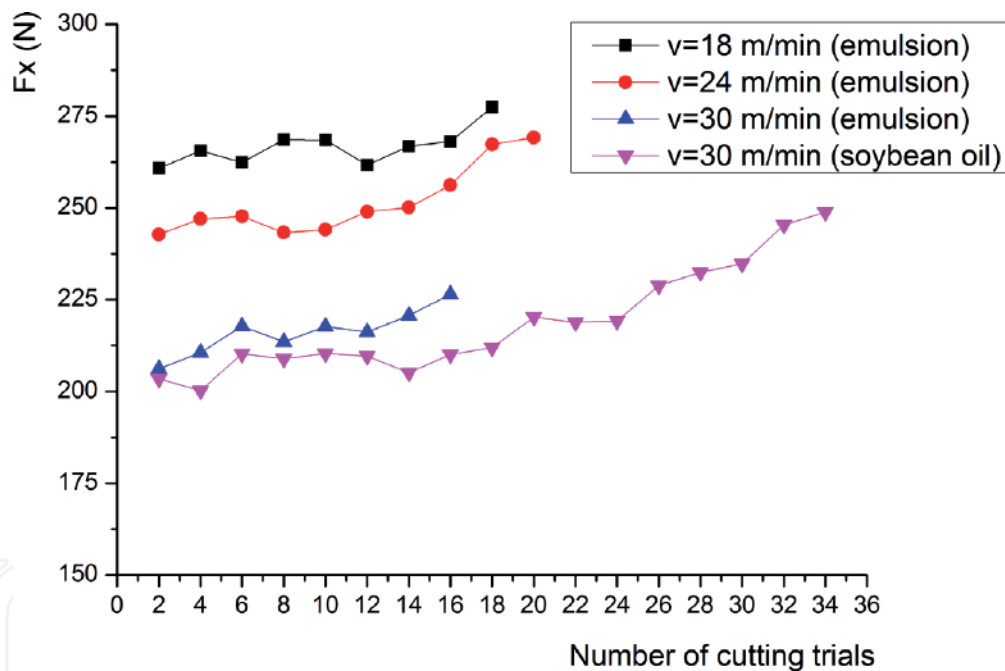


Figure 2.
The relation of cutting speeds and nanofluids to the cutting force F_x [16].

speeds from 18 to 30 m/min under MQL using emulsion. In addition to that, the burn marks caused by heat deterioration develop. It can be explained that SKD 11 tool steel has extremely high wear-resistant properties due to a high carbon and chromium (12% chrome) in chemical composition, from which it is grouped in difficult-to-cut material. In increasing the cutting speed from 18 to 30 m/min, MQL with emulsion-based fluid did not provide sufficient lubricating effects, so cutting temperature increased rapidly to damage end mills. In contrast, soybean oil has higher viscosity than that of emulsion, and the presence of Al_2O_3 nanoparticle additives contributes to improve the cooling and lubricating performance. Therefore, soybean oil-based nanofluid exhibits the superior lubricating effects to reduce friction coefficient in the cutting zone due to the easier formation of oil

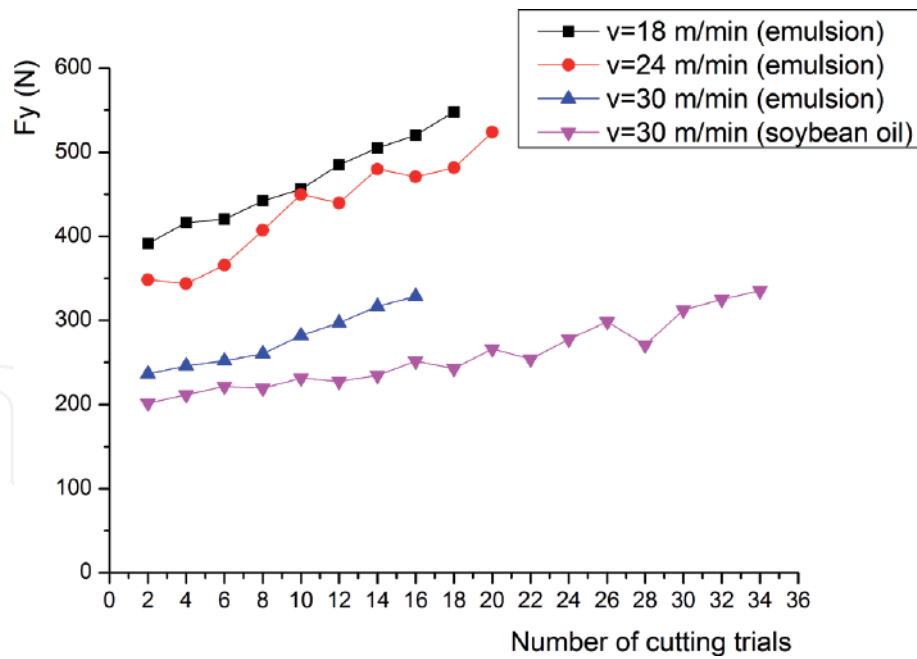


Figure 3.
 The relation of cutting speeds and nanofluids to the cutting force F_y [16].

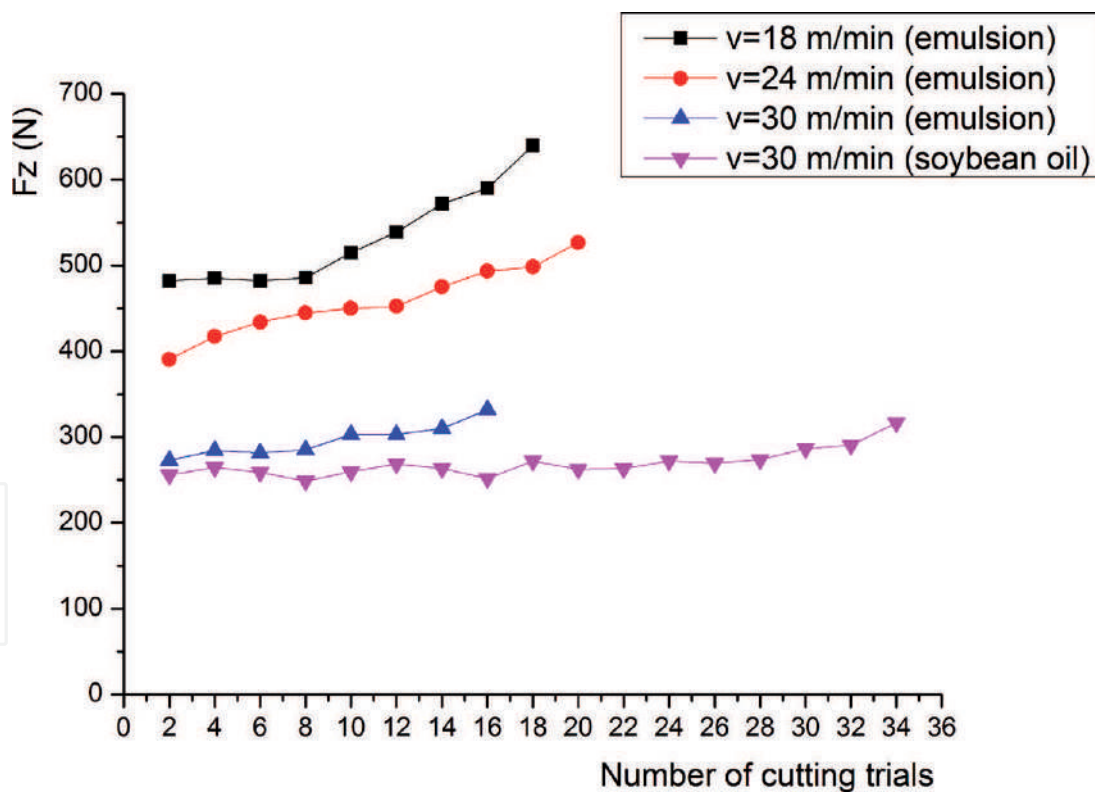


Figure 4.
 The relation of cutting speeds and nanofluids to the cutting force F_z [16].

mist. In this study of end milling process of SKD 11 steel before heat treatment, cutting heat did not exceed the ignition temperature of soybean oil. That is the main reason why MQL using soybean-based nanofluid is better in this situation. Furthermore, Al_2O_3 nanoparticles with nearly sphere morphology suspended in oil mist as “the rollers” play an important role in improving cooling and lubricating effects. From those reasons, notch wear and flank wear on HSS end mills at cutting speed $V_c = 30$ m/min significantly reduce. Notch and flank wear lands after 85 min

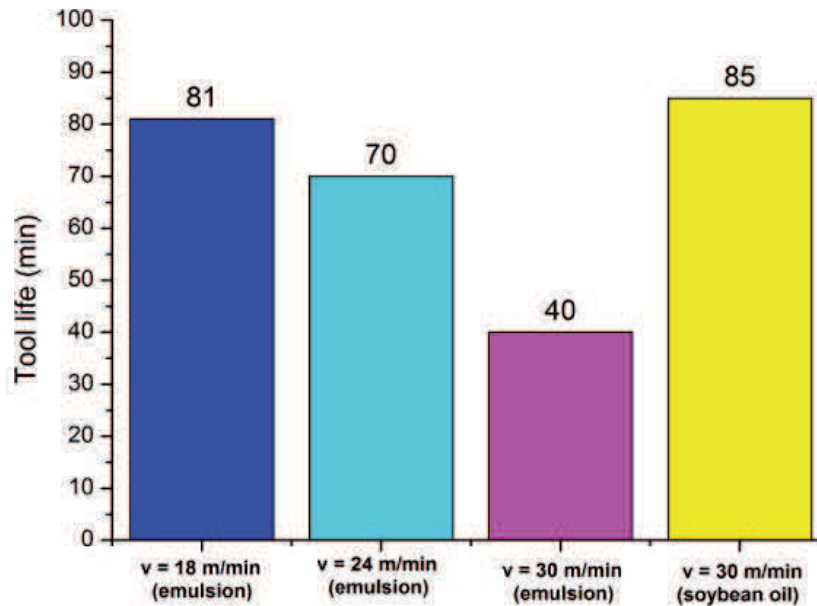


Figure 5.
The relation of cutting speeds and nano-cutting fluids to the tool life [16].

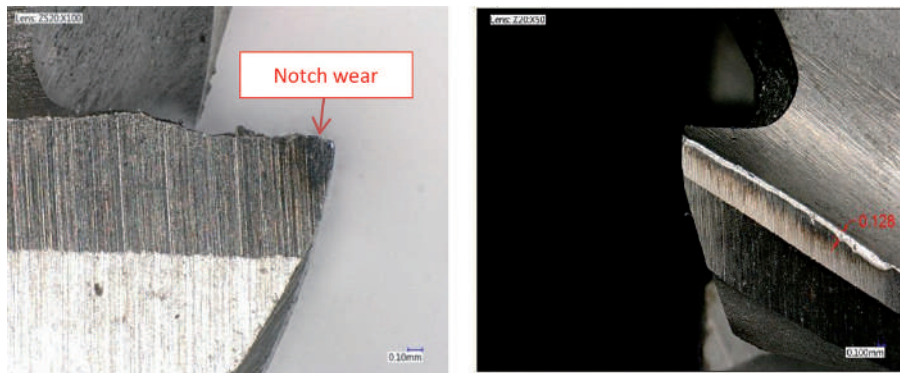


Figure 6.
Notch wear and flank wear ($V_c = 18$ m/min, emulsion-based nanofluid) [16].

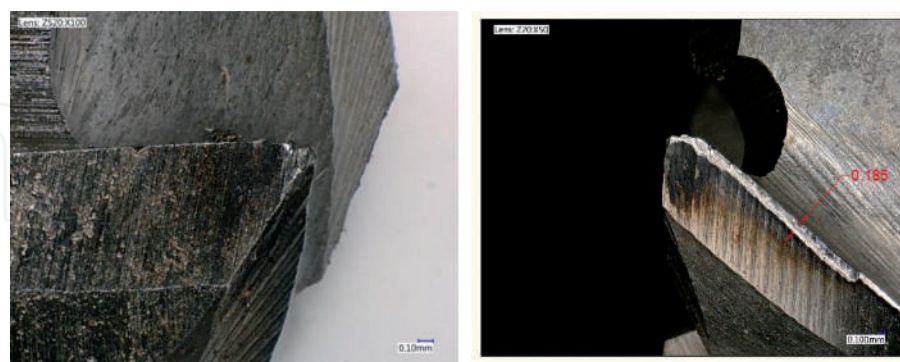


Figure 7.
Notch wear and flank wear ($V_c = 24$ m/min, emulsion-based nanofluid) [16].

of cutting are even lower than those of the case with MQL using emulsion-based nanofluid after 40 min of cutting (Figures 8–9). The significant reduction of burn marks indicates that the cooling and lubricating performance of soybean-based nanofluid is better and also suits for sustainable production due to the use of vegetable oil. Hence, tool life of end mill increases to 85 min even at cutting speed of 30 m/min, which is also higher than the manufacturers' recommendations [16]. According to ISO 8688-2:1989 (en) [17], the cutting speed for soft steels using

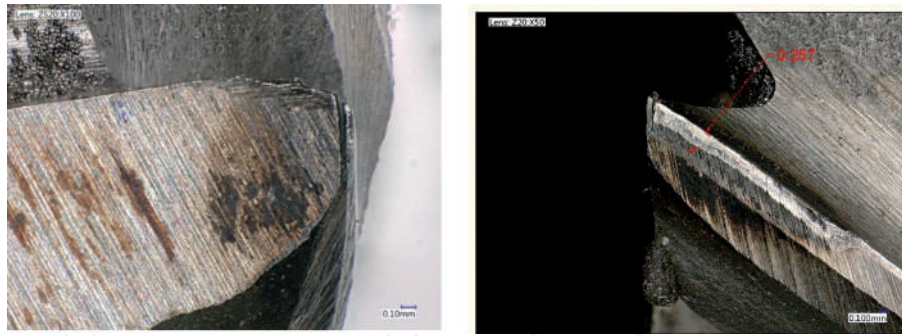


Figure 8.
Notch wear and flank wear ($V_c = 30$ m/min, emulsion-based nanofluid) at 40 min [16].



Figure 9.
Notch wear and flank wear ($V_c = 30$ m/min, soybean-based nanofluid) at 85 min [16].

normal HSS end mills is recommended about 30–35 m/min, but for difficult-to-cut steels like SKD 11, with hardness 200–250 HB, the cutting speed must be reduced to 14–18 m/min to ensure the proper cutting performance and tool life [18]. Moreover, the cutting speed also increases from 18 to 30 m/min by using MQL emulsion-based nanofluid, which reveals the better cooling and lubricating effects compared to the pure fluids.

2.2 The important parameter of MQL nanofluid

The concentration parameter of nanoparticles enriched in based fluids is among the most influential on machining outputs and costs, so it had been much studied to find out the appropriate and optimized values. Garg et al. [19] investigated the concentration effect of nanoparticles on micro-drilling process under MQL condition. The experimental results indicated that this parameter caused the significant reduction of drilling torque and power consumption. In the study of Lee et al. [20], the proper concentration of diamond nanoparticles was found with 0.05 wt%, from which the reduction of friction coefficient was observed by 23%. The authors concluded that diamond nanofluid provided the excellent anti-wear and lubricating effects. Zhang et al. [21] studied the concentration parameter of MoS_2 and CNT nano additives in MQL grinding. The improvement in lubricating performance contributes to increase surface quality. Furthermore, hybrid MoS_2 -CNT nanofluids provided the superior cooling lubrication compared to that of the fluid with a single type of nanoparticles. Luo et al. [22] studied Al_2O_3 nanoparticles enriched in MQL based fluid and concluded that Al_2O_3 nanofluid exhibited good resistant ability for high temperature. Then, the cutting temperature is not high to cause the reduction of wear rate, which is much smaller than that of dry condition. Yıldırım et al. [23] had done the study of MQL turning process of the difficult-to-cut steel Inconel 625 using hBN nano additives. The better lubricating performance

and surface roughness are reported from the obtained results, which led to reduce friction coefficient and wear rate. The authors also concluded that the optimal hBN nanoparticle concentration was 0.5 wt%. The experimental study on Al₂O₃ nanoparticle concentration used as MQL based fluid in hard milling had been done by using ANOVA analysis and response surface methodology (RSM), from which the research direction was made for optimizing the concentration variable [24]. **Figures 10–11** show the response surface plots of the relation of surface roughness and cutting force versus nano concentration (np), cutting speed V_c , and feed rate F . It can be clearly observed from **Figure 10** that, for better surface roughness, the low value of nanoparticle concentration about 0.5 wt% is more preferable than the larger ones (1.0 and 1.5 wt%). In contrast, the larger concentration (about 1.0 and 1.5 wt%) contributes to reduce the cutting forces and cutting temperature significantly when compared to the lower one (0.5 wt%). From those, the wear rate much reduces by increasing the concentration of Al₂O₃ nanoparticles to 1.0–1.5 wt%, so the tool life prolongs (**Figures 12–15**). Accordingly, the nanoparticle concentration must be chosen not only to ensure the good tool life but also to maintain the high surface quality.

From **Figure 13**, the chip colors are well matched with the reduction of cutting temperature. The dark purple and blue colors in the case of using $np = 0.5$ wt% change to brown and dark straw one in the case of using $np = 1.0–1.5$ wt%, which indicates that cutting temperature decreases [25]. It can be concluded that the decrease of coefficient of friction and generated heat is reported by increasing

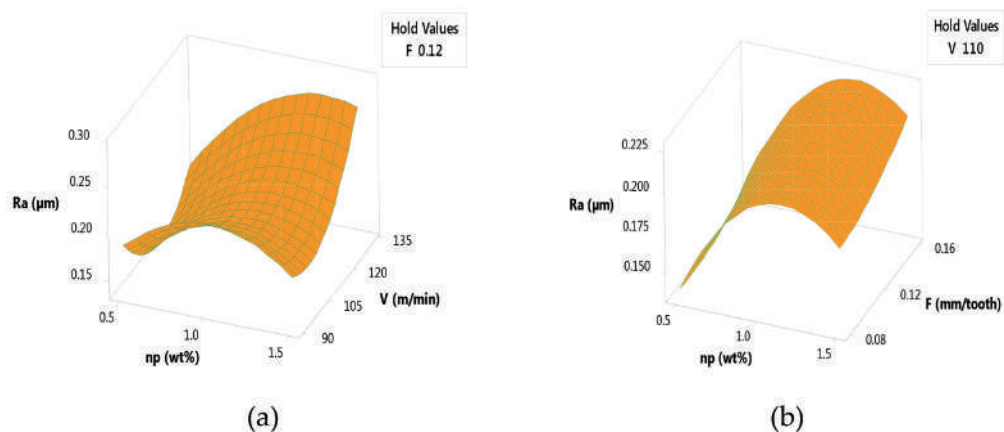


Figure 10. Response surface plots of surface roughness versus nano concentration and cutting speed (a), and nano concentration and feed rate (b) [24].

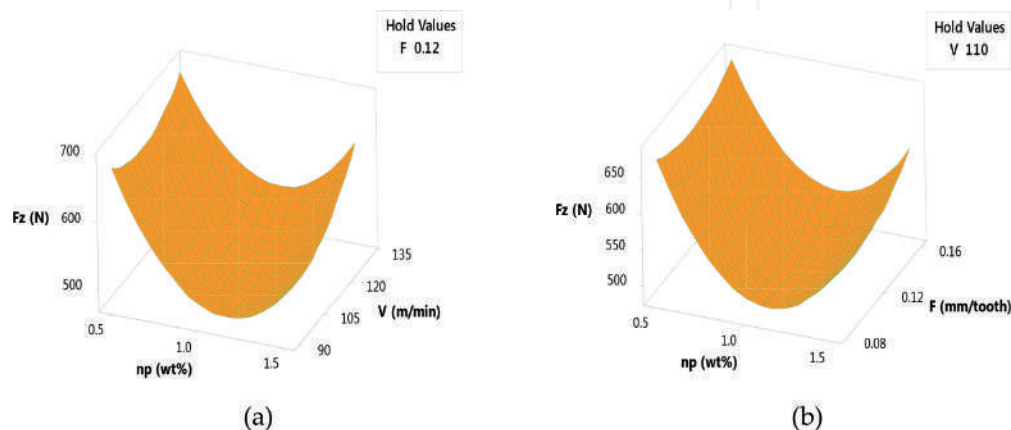


Figure 11. Response surface plots of cutting force F_z versus nano concentration and cutting speed (a), and nano concentration and feed rate (b) [24].

the concentration parameter of Al_2O_3 nanofluid, leading to reduce cutting forces and wear rate and prolong the tool life (**Figure 14**). From **Figure 15**, it clearly reveals that during the first 40 min, the values of surface roughness are higher when utilizing the high nanoparticle concentration (1.0–1.5 wt%). After that, the



(a)



(b)



(c)

Figure 12. Wear on flank face under MQL using soybean-based nanofluid at 80 min using different nano concentrations: (a) 0.5 wt%, (b) 1.0 wt%, and (c) 1.5 wt% [24].

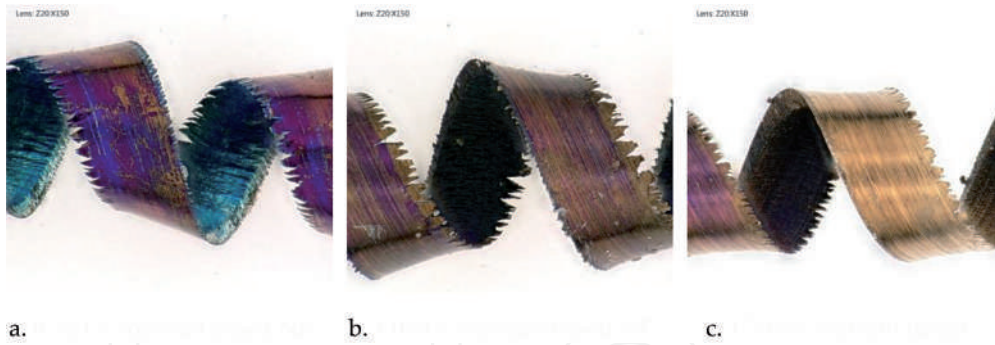


Figure 13. Chip colors and micrographs with different Al_2O_3 nanoparticle concentrations (at 80 min): (a) 0.5 wt%, (b) 1.0 wt%, and (c) 1.5 wt% [24].

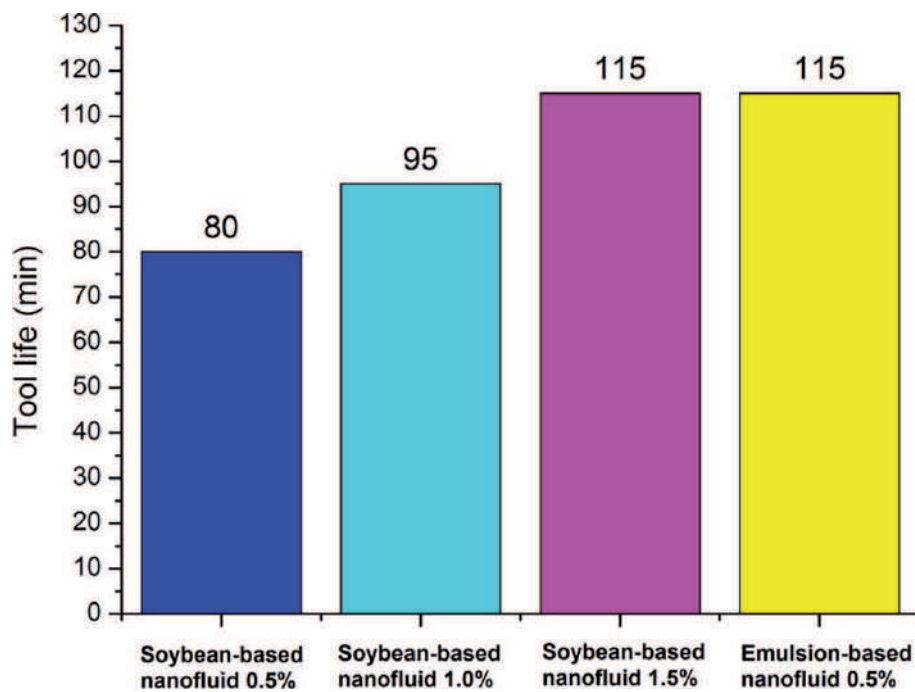


Figure 14. Tool life with different Al_2O_3 nanoparticle concentrations [24].

rate of reduction of surface roughness values rapidly increases, which is contrary to the case of using 0.5 wt%. It is the novel observation obtained from the validation experiments, which is conducted until the tool life ends to see the actual phenomena after receiving the ANOVA and RSM results. Interestingly, the tool life in the case of soybean-based nanofluid 1.5 wt% is equal to that of emulsion-based nanofluid 0.5 wt%. It provides an important technical guide to enlarge the applicability of vegetable oil-based nanofluid in hard cutting processes as well as maintains its environmental-friendly characteristics.

However, each type of nanoparticles has its own specific morphology and property, so the appropriate or optimal concentration parameters are different [26]. This is the up-to-date research topic. Accordingly, more investigations are needed to make and build up the technical guides for manufacturers in machining practice, even though many studies have been done to optimize these variables. In order to develop MQL method, minimum quantity cooling lubrication (MQCL) has been considered as another promising approach to solve the low cooling performance, the main MQL drawback. It is also the newest research topic, which is discussed in Sections 3 and 4.

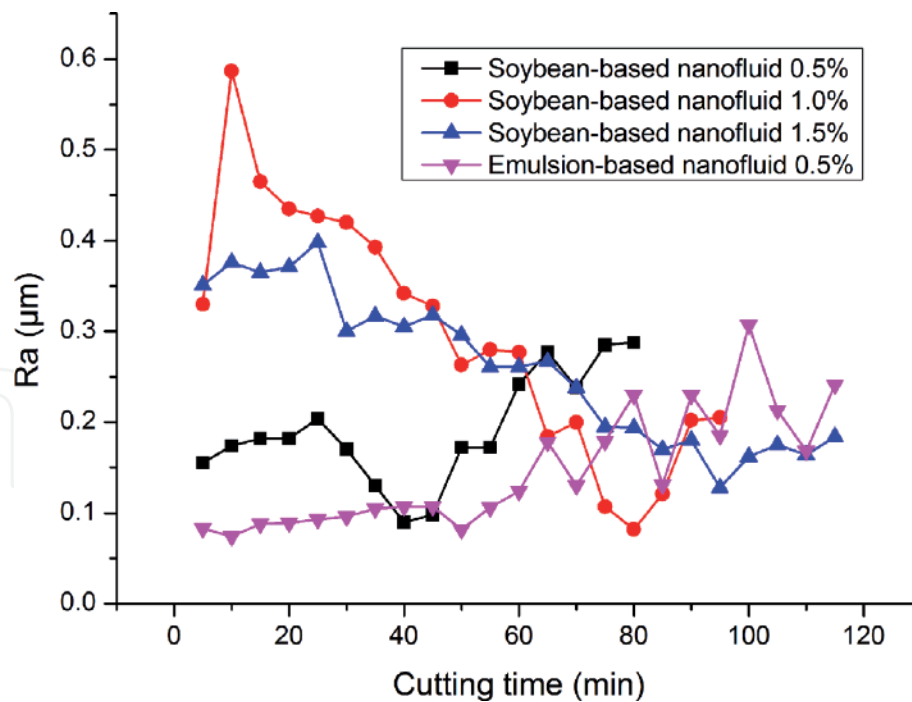


Figure 15. Surface roughness Ra with different Al_2O_3 nanoparticle concentrations [24].

3. Hard machining under MQCL condition

The large amount of heat generated from hard cutting is always the big challenge for selecting cutting tools and cutting condition while ensuring the technical requirements, productivity, and proper manufacturing cost. Hence, providing appropriate cooling and lubricating effects to cutting zone plays a vital role in the development of hard machining processes. The applicability of those can be enlarged to some or all of the traditional grinding processes. MQCL technique has been proposed and developed to fulfill the cooling and lubricating requirements and is also a solution for improving MQL method. Up to now, MQCL has drawn much attention and has been studied in recent years. Maruda et al. [27, 28] made the study on MQCL parameters using emulsion-based fluid in hard turning process. The obtained results indicated that emulsion oil mist formed under MQCL condition plays an important role for improving the cooling lubricating performance in the cutting zone and increasing the cutting condition. The formation of tribo-films tends to occur easily with the droplets with smaller size, which help to decrease the coefficient of friction, cutting forces, and wear rate [29, 30]. The better cooling and lubricating effects of MQCL technique also reflect through the chip shape and the reduction of chip thickening coefficient [31]. Pervaiz and his co-authors [32] studied MQCL performance in the turning process of difficult-to-cut material Ti6Al4V. The author concluded that cutting forces and tool wear reduced and surface quality improved when compared to dry and flood conditions. It reveals the better cooling and lubricating effects of MQCL technique. Krolczyk together with his co-authors [33] investigated the parametric and nonparametric description of the surface topography under dry and MQCL conditions using emulsion-base fluid. The study results showed that the nozzle distance causes the strongest influence on droplet diameter. The most outstanding finding of this research is that parameters can be chosen for oil mist formation in a certain time, which is enough for creating cooling and lubricating effects and then evaporating due to generated heat from the cutting zone. Based on a brief review, it can be clearly seen that there is little information of MQCL technique and most of the studies relied on the based fluid

having cooling effect like emulsion oil to form MQCL method. The use of a real cooling method assisted to MQL technique to form MQCL condition is a novel approach. In this section, the author presents the newest advances in using the principle of Ranque-Hilsch vortex tube for separating a compressed gas into hot and cold streams from ordinary air [34], in that the cold stream is used to create cooling effects combined with MQL method to form MQCL [35]. The deep study on hard milling of SKD 11 steel (52–60 HRC) in terms of surface quality under MQCL condition was done, and the results were compared to dry and MQL conditions. From **Figure 16**, hard milling under MQCL method brought out better surface roughness than those under dry and MQL conditions. The main reason is that MQCL technique provides sufficient cooling and lubricating effects, especially cooling effect, which helps to reduce the cutting temperature and tool wear.

KEYENCE VHX-6000 Digital Microscope (Keyence Corporation, Osaka, Japan) was utilized for studying surface microstructure and surface profile (**Figure 17**). The

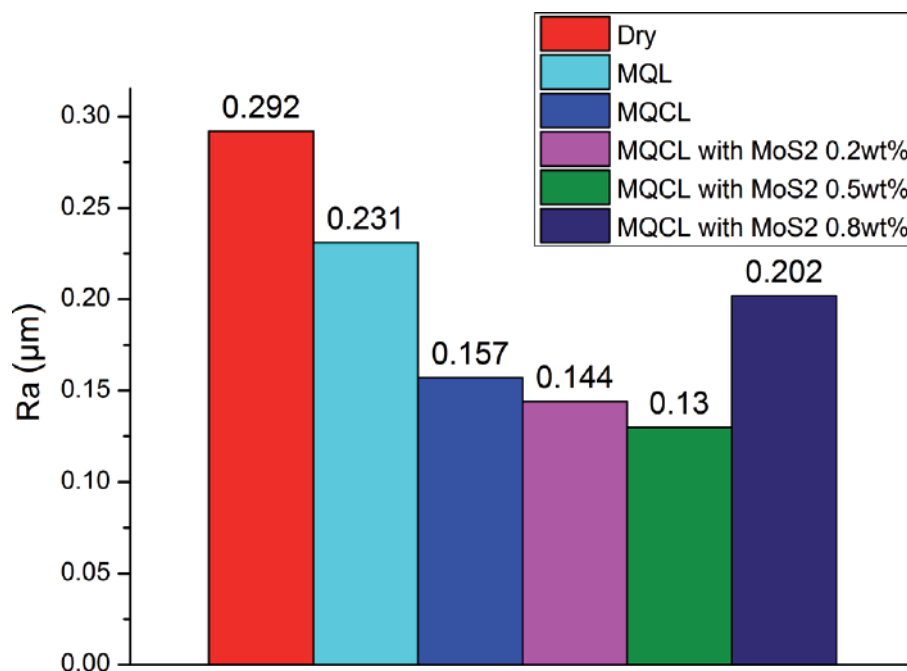


Figure 16.

The average values of surface roughness R_a under different cooling and lubricating conditions (cutting speed $V_c = 110$ m/min, feed rate $F = 0.012$ mm/tooth, depth of cut $d = 0.12$ mm, hardness of 56 HRC) [35].

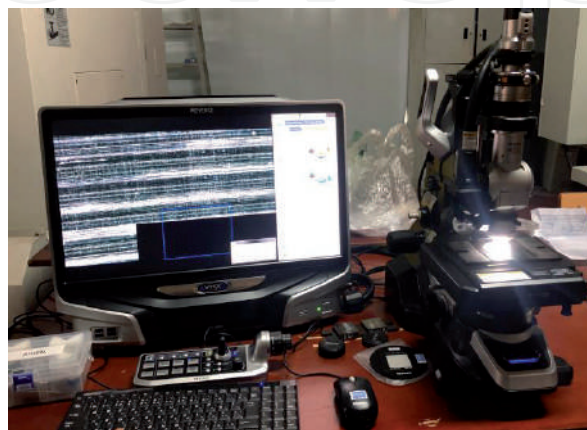


Figure 17.

KEYENCE VHX-6000 digital microscope for studying machined surface topography.

machined surfaces under different cooling and lubricating conditions are investigated (Figures 18–22). The white layer and burn marks significantly reduced under MQL and MQCL conditions compared to dry cutting because of cooling and lubricating enhancement. The burn marks under MQCL condition are less than those under MQL method due to better cooling performance (Figures 19(a), 20(a)). In addition, compared to dry and MQL conditions, the compression of machined surface observed from the surface profile much reduces (Figures 18(b), 19(b), 20(b)).

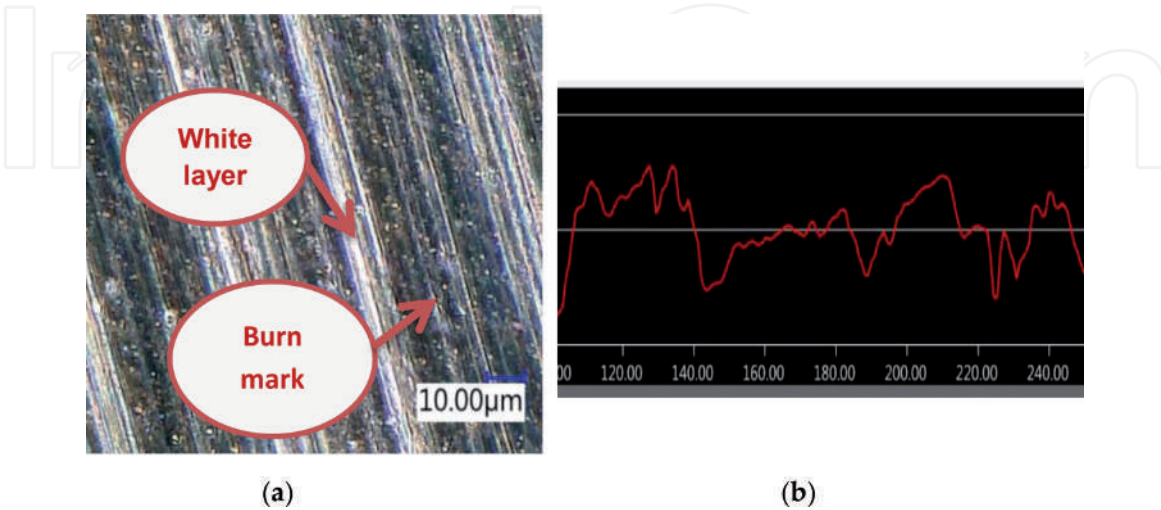


Figure 18.
Surface microstructure (a) and profile (b) under dry condition [35].

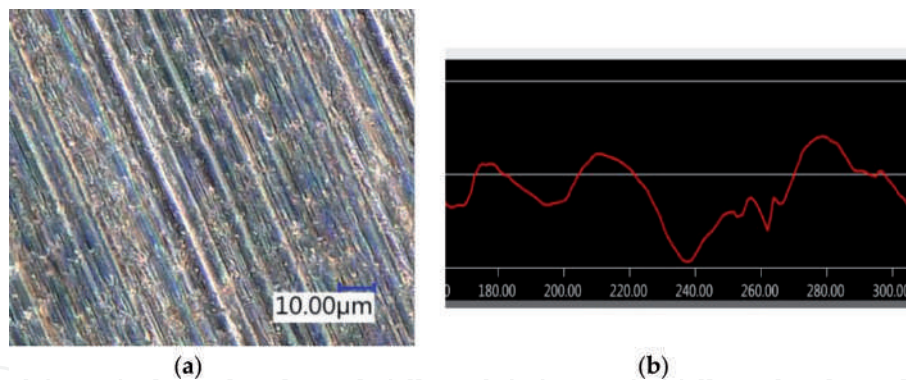


Figure 19.
Surface microstructure (a) and profile (b) under MQL condition [35].

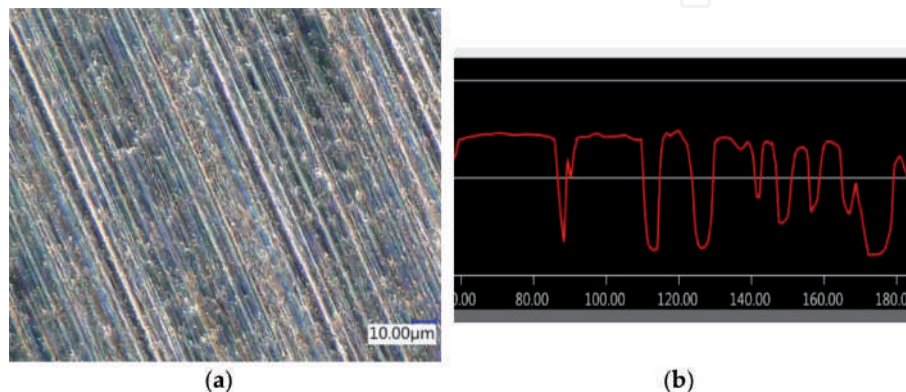


Figure 20.
Surface microstructure (a) and profile (b) under MQCL condition using pure emulsion-based fluid [35].

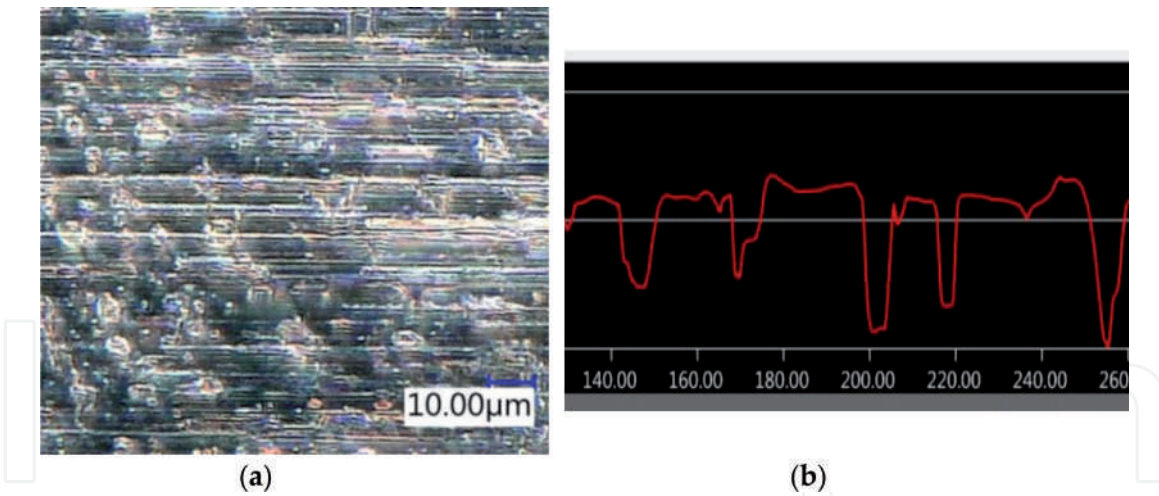


Figure 21. Surface microstructure (a) and profile (b) under MQCL condition using emulsion-based nanofluid of MoS₂ 0.2 wt% [35].

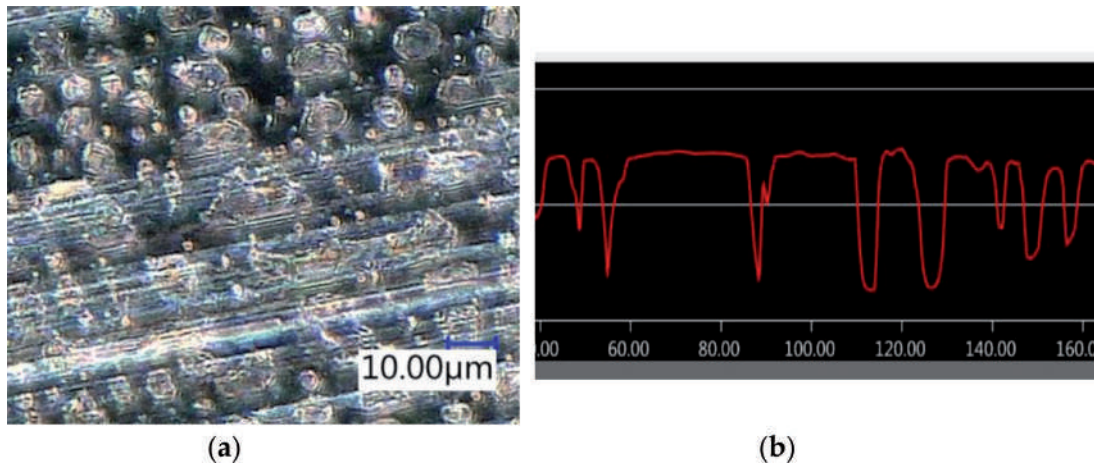


Figure 22. Surface microstructure (a) and profile (b) under MQCL condition using emulsion-based nanofluid of MoS₂ 0.5 wt% [35].

4. MQCL hard machining using nanofluids

The nanofluids used for MQL are successfully proven to be an alternative solution for difficult-to-cut materials while maintaining its environmental friendly property. Based on this idea, the use of nano additives in MQCL method will bring out the promising solution to increase the hard machining performance. The study of surface quality under MQCL using MoS₂ nanofluid for hard milling is the first attempt to investigate the cooling and lubricating effects [35]. From the obtained results, the values of surface roughness R_a under MQCL using nanofluids are lower than those of dry and MQL conditions. By using MoS₂ nanoparticle concentration of 0.2 and 0.5 wt%, surface roughness is even slightly better than that of MQCL with pure fluid, but the R_a value rapidly increases when increasing the concentration to 0.8 wt%. It can be explained that the morphology of MoS₂ nanoparticles is ellipsoidal with the low friction coefficient up to 0.03–0.05 or even lower [36], by which the better lubricating effect contributes to improve the surface quality. On the other hand, nanoparticles possess the large surface area, which remain on the machined surface to form a thin protective film, which amplifies with the increase of MoS₂ nanoparticle concentration [37]. Furthermore, it also contributes to form MoS₂ tribo-film easily [29],

which can be observed from the so-called microbubbles on the machined surface (Figures 21–22). The protective film reduces and disappears when increasing the concentration to 0.8%, which causes the negative effect on surface quality [37]. Moreover, the white layer and burn marks are much reduced due to superior cooling and lubricating performance under MQCL condition using nanofluid. From those, the hard machining ability of normal carbide tools improves significantly and is about 157% higher than manufacturer's recommendations [38, 39]. It is the most outstanding finding of this research, and also the proper MoS₂ nanoparticle concentration in emulsion-based fluid was reported about 0.2 and 0.5 wt%, which provides a very important technical guide for further researches and manufacturers. More investigations are necessary to be made for building up technical guidelines and optimizing nanofluid parameters.

5. Conclusion

The application of nanofluids continues to receive growing attention in basic science and machining technology. As shown, nano additives in based fluid of MQL and MQCL methods improve the cooling and lubricating effects as well as tribological property, thus increasing the cutting performance, especially for difficult-to-cut materials. It brings out the alternative solutions for improving productivity and reducing manufacturing cost. From those, the applicability MQL technique having environmental friendly characteristic has been enlarged in hard machining. Furthermore, the use of different types of vegetable oils can fulfill the cooling and lubricating performance by suspending nanoparticles, which is an interesting research topic and exhibits very promising results. On the other hand, MQCL has been considered as another approach for MQL development to overcome the low cooling effect. In this chapter, Ranque-Hilsch vortex tube, a real cooling method, used for creating cooling effect from ordinary compressed air rather than other gas sources to form MQCL method, is the first attempt applied to hard cutting processes. Also, nano additives enriched in MQCL-based fluids are the latest advances in the field of studying MQL and MQCL techniques. The parameters of nanofluid, such as types and size of nanoparticles, concentration, and based fluid, play a key role in successful applications in metal cutting practice, and more studies are needed to make further development and optimize those variables. Those superior cooling and lubricating methods presented in this chapter will contribute to the solutions to reduce/eliminate the cutting fluids and replace dry and wet conditions. It is suitable for protecting our environment and aims for a sustainable production. In the future work, more attention will be paid on other types of nanoparticles, concentration, and parameters of MQL and MQCL methods.

Acknowledgements

The work presented in this chapter is supported by Thai Nguyen University of Technology, Thai Nguyen University, Vietnam.

Conflict of interest

The authors declare no conflict of interest.

Acronyms and abbreviations

d	depth of cut (mm)
V_c	cutting speed (m/min)
F	feed rate (mm/tooth)
F	cutting force (N)
HSS	high speed steel
hBN	hexagonal boron nitride
CNTs	carbon nanotubes
ML	minimum quantity lubrication
MQCL	minimum quantity cooling lubrication
NFMQL	nanofluid minimum quantity lubrication
ND	nanodiamond
NF	nanofluid
NFs	nanofluids
NP	nanoparticle
NPs	nanoparticles
ANOVA	analysis of variance

Author details

Tran The Long* and Tran Minh Duc
Department of Manufacturing Engineering, Faculty of Mechanical Engineering,
Thai Nguyen University of Technology, Vietnam

*Address all correspondence to: tranthelong@tnut.edu.vn;
tranthelong90@gmail.com

IntechOpen

© 2020 The Author(s). Licensee IntechOpen. This chapter is distributed under the terms
Commons Attribution - NonCommercial 4.0 License (<https://creativecommons.org/licenses/by-nc/4.0/>), which permits use, distribution and reproduction for
non-commercial purposes, provided the original is properly cited. 

References

- [1] Byrne G, Dornfeld D, Denkena B. Advancing cutting technology. *CIRP Annals*. 2003;**52**(2):483-507
- [2] Zhang K, Deng J, Meng R, Gao P, Yue H. Effect of nano-scale textures on cutting performance of WC/Co-based Ti55Al45N coated tools in dry cutting. *International Journal of Refractory Metals and Hard Materials*. 2015;**51**:35-49
- [3] Paulo DJ. *Machining of Hard Materials*. London: Springer-Verlag London Limited; 2011
- [4] Kumar CS, Patel SK. Effect of WEDM surface texturing on Al₂O₃/TiCN composite ceramic tools in dry cutting of hardened steel. *Ceramics International*. 2018;**44**:2510-2523
- [5] Su Y, Li Z, Li L, Wang J, Gao H, Wang G. Cutting performance of micro-textured polycrystalline diamond tool in dry cutting. *Journal of Manufacturing Processes*. 2017;**27**:1-7
- [6] S N, G.L S. Drilling performance of micro textured tools under dry, wet and MQL condition. *Journal of Manufacturing Processes*. 2018;**32**:254-268. DOI: 10.1016/j.jmapro.2018.02.012
- [7] Minh DT, The LT. Investigation of MQL-employed hard-milling process of S60C steel using coated-cemented carbide tools. *Journal of Mechanics Engineering and Automation*. 2016;**6**:128-132
- [8] Rahim EA, Sasahara H. A study of the effect of palm oil as MQL lubricant on high speed drilling of titanium alloys. *Tribology International*. 2011;**44**:309-317
- [9] Duc TM, Long TT, Ngoc TB. Performance of Al₂O₃ nanofluids in minimum quantity lubrication in hard milling of 60Si₂Mn steel using cemented carbide tools. *Advances in Mechanical Engineering*. 2017;**9**:1-9
- [10] Long TT, Duc TM. Micro/Nanofluids in Sustainable Machining. In: *Microfluidics and Nanofluidics*. London, UK: IntechOpen; 2018
- [11] Lee P-H, Nam JS, Li C, Lee SW. An experimental study on micro-grinding process with nanofluid minimum quantity lubrication (MQL). *International Journal of Precision Engineering and Manufacturing*. 2012;**13**:331-338
- [12] Li B, Li C, Zhang Y, Wang Y, Jia D, Yang M, et al. Heat transfer performance of MQL grinding with different nanofluids for Ni-based alloys using vegetable oil. *Journal of Cleaner Production*. 2017;**154**:1-11
- [13] Ali MKA, Hou X, Mai L, Cai Q, Turkson RF, Chen B. Improving the tribological characteristics of piston ring assembly in automotive engines using Al₂O₃ and TiO₂ nanomaterials as nano-lubricant additives. *Tribology International*. 2016;**103**:540-554
- [14] Pashmforoush F, Bagherinia RD. Influence of water-based copper nanofluid on wheel loading and surface roughness during grinding of Inconel 738 superalloy. *Journal of Cleaner Production*. 2018;**178**:363-372
- [15] Uysal A, Demiren F, Altan E. Applying minimum quantity lubrication (MQL) method on milling of martensitic stainless steel by using nano MoS₂ reinforced vegetable cutting fluid. *Procedia - Social and Behavioral Sciences*. 2015;**195**:2742-2747
- [16] Duc TM, Long TT, Ngoc TB. Effectiveness of alumina nanofluid on slotting end milling performance of SKD 11 tool steel. *Journal of Computational and Applied Research in Mechanical Engineering*. 2019. DOI: 10.22061/JCARME.2019.4041.1484

- [17] ISO 8688-2:1989 (en). Tool life testing in milling — Part 2: End milling; 1989. pp. 9-14
- [18] Duc TM, Dong PQ. Influence of coolant fluid and method on tool wear, tool life and the surface roughness in slot machining using end mills. *Journal of Science and Technology Technical Universities*. 2008;**65**:55-58
- [19] Garg A, Sarma S, Panda B, Zhang J, Gao L. Study of effect of nanofluid concentration on response characteristics of machining process for cleaner production. *Journal of Cleaner Production*. 2016;**135**:476-489
- [20] Lee G-J, Park J-J, Lee M-K, Rhee CK. Stable dispersion of nanodiamonds in oil and their tribological properties as lubricant additives. *Applied Surface Science*. 2017;**415**:24-27
- [21] Zhang Y, Li C, Jia D, Li B, Wang Y, Yang M, et al. Experimental study on the effect of nanoparticle concentration on the lubricating property of nanofluids for MQL grinding of Ni-based alloy. *Journal of Materials Processing Technology*. 2016;**232**:100-115
- [22] Luo T, Wei X, Huang X, Huang L, Yang F. Tribological properties of Al₂O₃ nanoparticles as lubricating oil additives. *Ceramics International*. 2014;**40**:7143-7149
- [23] Yıldırım ÇV, Sarıkaya M, Kivak T, Şirin Ş. The effect of addition of hBN nanoparticles to nanofluid-MQL on tool wear patterns, tool life, roughness and temperature in turning of Ni-based Inconel 625. *Tribology International*. 2019;**134**:443-456
- [24] Duc TM, Long TT, Dong PQ. Effect of the alumina nanofluid concentration on minimum quantity lubrication hard machining for sustainable production. *Proceedings of the Institution of Mechanical Engineers, Part C: Journal of Mechanical Engineering Science*. 2019;**233**(17):5977-5988. DOI: 10.1177/0954406219861992
- [25] Oberg E, Jones F, Horton H, Ryffel H, McCauley C. *Machinery's Handbook*. 30th Edition, Toolbox ed. United States: Industrial Press; 2016. ISBN: 9780831130916
- [26] Duc TM, Long TT, Chien TQ. Performance evaluation of MQL parameters using Al₂O₃ and MoS₂ nanofluids in hard turning 90CrSi steel. *Lubricants*. 2019;**7**(5):1-17. DOI: 10.3390/lubricants7050040
- [27] Maruda RW, Krolczyk GM, Feldshtein E, Nieslony P, Tyliszczak B, Pusavec F. Tool wear characterizations in finish turning of AISI 1045 carbon steel for MQCL conditions. *Wear*. 2017;**372**:54-67
- [28] Maruda RW, Krolczyk GM, Feldshtein E, Pusavec F, Szydłowski M, Legutko S, et al. A study on droplets sizes, their distribution and heat exchange for minimum quantity cooling lubrication (MQCL). *International Journal of Machine Tools and Manufacture*. 2016;**100**: 81-92
- [29] Maruda RW, Krolczyk GM, Wojciechowski S, Zak K, Habrat W, Nieslony P. Effects of extreme pressure and anti-wear additives on surface topography and tool wear during MQCL turning of AISI 1045 steel. *Journal of Mechanical Science and Technology*. 2018;**32**:1585-1591
- [30] Maruda RW, Feldshtein E, Legutko S, Krolczyk GM. Research on emulsion mist generation in the conditions of minimum quantity cooling lubrication (MQCL). *Tehnicki Vjesnik*. 2015;**22**:1213-1218
- [31] Maruda R, Krolczyk G, Nieslony P, Krolczyk J, Legutko S, Krolczyk G. Chip

formation zone analysis during the turning of austenitic stainless steel 316L under MQCL cooling condition. *Procedia Engineering*. 2016;**149**:297-304

[32] Pervaiz S, Deiab I, Rashid A, Nicolescu M. Minimal quantity cooling lubrication in turning of Ti6Al4V: Influence on surface roughness, cutting force and tool wear. *Proceedings of the Institution of Mechanical Engineers, Part B: Journal of Engineering Manufacture*. 2017;**231**:1542-1558. DOI: 10.1177/0954405415599946

[33] Krolczyk G, Maruda R, Krolczyk J, Nieslony P, Wojciechowski S, Legutko S. Parametric and nonparametric description of the surface topography in the dry and MQCL cutting conditions. *Measurement*. 2018;**121**:225-239

[34] Hilsch R. The use of the expansion of gases in a centrifugal field as cooling process. *The Review of Scientific Instruments*. 1947;**18**(2):108-113

[35] Dong PQ, Duc TM, Long TT. Performance evaluation of MQCL hard milling of SKD 11 tool steel using MoS₂ nanofluid. *Metals*. 2019;**9**:658. DOI: 10.3390/met9060658

[36] Wang Y, Li C, Zhang Y, Li B, Yang M, Zhang X, et al. Experimental evaluation of the lubrication properties of the wheel/workpiece interface in MQL grinding with different nanofluids. *Tribology International*. 2016;**99**:198-210

[37] Rahmati B, Sarhan AA, Sayuti M. Morphology of surface generated by end milling AL6061-T6 using molybdenum disulfide (MoS₂) nanolubrication in end milling machining. *Journal of Cleaner Production*. 2014;**66**:685-691

[38] Available from: <https://wix.laminattech.ch/img/catalog/1237.pdf>

[39] Duc TM, Long TT, Dong PQ, Ngoc TB. Applied research of Nanofluids in MQL to improve hard milling performance of 60Si₂Mn steel using carbide tools. *American Journal of Mechanical Engineering*. 2017;**5**(5):228-233. DOI: 10.12691/ajme-5-5-6